ABSTRACT

INVESTIGATION OF LASER SPECKLE CONTRAST IMAGING'S SENSITIVITY TO FLOW

by Anthony Milard Young

This thesis presents data from a series of experiments that investigate the ability of laser speckle contrast imaging (LSCI) to sense changes in flow in turbid media. I first provide a theoretical overview and a description of the experimental approach used in this flow imaging technique. Experimental validation of the technique's ability to sense induced changes in blood flow in the human forearm is demonstrated. Then, the technique's sensitivity to buried flow in controlled optical phantoms is examined. It is shown that the buried depth and optical properties of the media surrounding flow impact the measured flow indices. Lastly, a study shows how the polarization state of the imaged light impacts the flow measurements as a function of the buried depth and rate of the flow. The results demonstrate that the measurements are dependent on the flow rates and optical properties of the sample as well as the imaging setup used to capture the speckle.

INVESTIGATION OF LASER SPECKLE CONTRAST IMAGING'S SENSITIVITY TO FLOW

A Thesis

Submitted to the

Faculty of Miami University

in partial fulfillment of

the requirements for the degree of

Master of Science

by

Anthony Milard Young

Miami University

Oxford, Ohio

2018

Advisor: Dr. Karthik Viswanath

Reader: Dr. Paul Urayama

Reader: Dr. E. Carlo Samson

This Thesis titled

INVESTIGATION OF LASER SPECKLE CONTRAST IMAGING'S SENSITIVITY TO FLOW

by

Anthony Milard Young

has been approved for publication by

The College of Arts and Science

and

Department of Physics

_____

Dr. Karthik Vishwanath

_____

Dr. Paul Urayama

_____

Dr. E. Carlo Samson

Table of Contents

List of Tables

List of Figures

Dedication

To my parents, Lisa and John, for the support that you have shown me. You raised me with love and taught me the importance of a good education, work ethic, and compassion. Without these, this work would not have been possible.

Acknowledgement

I would like to first thank my adviser, Dr. Karthik Vishwanath, for his support and guidance through both my undergraduate and graduate education. I am forever thankful for the opportunities that he has given me and all the lessons that he has taught me over the years. Additionally, I would like to thank all the members of the OSIM lab. They have been excellent lab mates and friends who it has been a pleasure to work alongside. Special thanks go to my fellow lab member, Sara Zanfardino who I worked alongside while conducting much of the work in this thesis. She has been an excellent friend during the completion of this degree.

Next, I thank Dr. Paul Urayama for serving as a mentor throughout the past few years. Thanks also go to him, Dr. Carlo Samson, and Dr. Perry Rice for the time that they have given to constructively critique this work. These individuals along with the rest of the faculty and staff of the Department of Physics at Miami have given me all the support that made this work possible.

Finally, I thank my family for their encouragement and constant belief in me throughout my life.

Chapter 1– Introduction and Background

1.1- Introduction

Next time you pick up a laser-pointer, shine it at a wall or piece of paper and observe the light that is scattered back to your eye. What you will see is a high-contrast, grainy appearance of the light that is captured on the back of your retina. This grainy pattern that is made of bright and dark spots is known as “speckle” [1].

Speckle is the resulting interference pattern that is formed when coherent light, emanating from a laser, is scattered from an optically rough medium. A medium is considered optically rough when the scattering particles are randomly distributed on a scale equal to or larger than the wavelength of the illuminating light [2]. A point on an imaging plane will receive an ensemble of photons that have been scattered from various positions within the scattering medium. The random distribution of path lengths traveled by the photons reaching that point translates into random phases of the electric field. When the randomly phased component fields interfere constructively, a bright spot is seen. If the fields of the randomly-phased photons sum to zero, a dark spot is observed. The resulting image will consist of a spatially random intensity pattern, the defining characteristic of speckle as shown in Figure 1 [2-4].

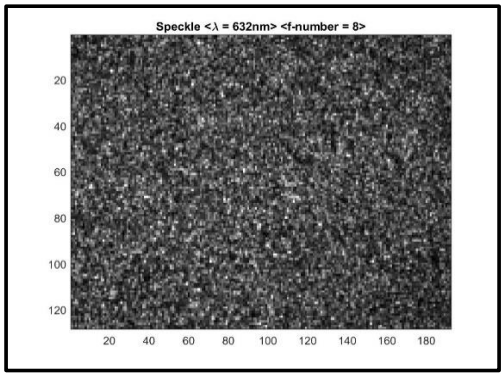

Figure 1. *This figure displays an example of a speckle pattern scattered from a static medium. The image was captured under illumination by a 633 nm HeNe laser and a numerical aperture of 8. The axes indicate the position in pixel units.*

Speckle is often observed in optics because most surfaces and media are optically rough (the obvious exception being mirrors). This has historically been considered a negative, and there have been many studies of methods to suppress this noise [1, 4]. However, it has been realized that speckle can be useful as a tool to detect movement or flow [5].

When particles scattering coherent light move, the intensity of the speckle will fluctuate in time. These fluctuations can be captured when the speckle is imaged over a finite exposure time. Because the frequency of the fluctuations depends on the velocity of the scatterers, information about their velocity is encoded in the captured image [4]. This information can be assessed through the contrast of the speckle in the image. The speckle contrast K is defined as the ratio of the standard deviation σ_I and the mean intensity $\langle I \rangle$ of the image [6]

$$K = \frac{\sigma_I}{\langle I \rangle}. \tag{1.1}$$

This ratio quantifies the amount of blurring of the speckle that occurs as the intensity fluctuates over the exposure time of the camera [4]. If the illuminated sample is static, the speckles will not blur, and the image will have a high contrast. This contrast will be reduced if the speckles blur due to movement of the scatterers as demonstrated in Fig. 2.

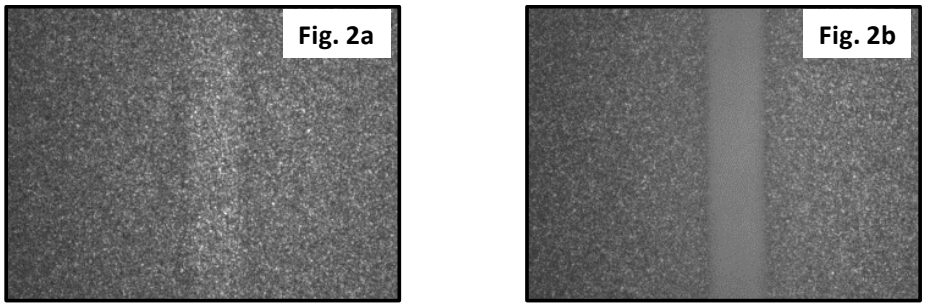

Figure 2. *This figure shows an experimental representation of a decrease in contrast due to a flowing, scattering medium. These are raw speckle images of a transparent tube containing a scattering medium that is surrounded by another scattering fluid captured with an exposure time of 10ms under 633 nm illumination. The fluid in the tube on the left (Fig. 2a) has no directional flow, while the tubing on the right (Fig. 2b) has a directional flow of 6 mL/min through it.*

The relationship between speckle contrast and flow has been used to develop a wide-field, non-contact method for flowing imaging known as laser speckle contrast imaging (LSCI)[4, 7, 8]. In this thesis, I present the progress that was made to investigate LSCI's sensitivity to flow of turbid media.

1.2- Thesis Organization

The rest of Chapter 1 is used to describe the theory and history needed to understand laser speckle contrast imaging. I first present the theory that explains the formation and statistics of speckle patterns and that which relates dynamic speckle to the velocity of scatterers. A brief historical description of LSCI and its applications is also presented.

Chapter 2 is used to describe the experimental approach that was used to capture and analyze speckle images for various applications. Experimental results and discussion are presented in Chapter 3 through 5. The order of these chapters follows the chronological order in which the individual studies were completed. Chapter 3 summarizes a study that provided experimental data that verified that our LSCI setup can sense changes in blood flow rates *in vivo*. Chapter 4 investigates LSCI's depth sensitivity to flow buried beneath a scattering media. Chapter 5 provides an experimental examination of the effect polarization has on LSCI's depth-sensitivity to flow. Following these chapters, Chapter 6 is used to describe the outlook of the work that was accomplished. Finally, concluding remarks are provided in Chapter 7.

1.3- Introduction to Speckle

In this section, a brief explanation of the model that explains the formation and statistics of static speckle that is useful to understanding laser speckle contrast imaging is provided. Goodman provides a complete text on the field of speckle in *Speckle Phenomena in Optics: Theory and Applications* [9]. The text has become a great resource to gain a deeper understand of the statistical properties of speckle as well as a wide range of applications in which speckle plays an important role. The following section summarizes the statistical model of speckle that Goodman provides in the text [9].

1.3.1- Modeling Static Speckle

To create a model of speckle, the object under coherent illumination can be modeled as an array of a very large number, *N*, of point sources of light at the object plane of the imaging system [10]. Each point source produces an electromagnetic wave with a specific diffraction pattern (an Airy disk for systems with circular apertures [11]) on the imaging plane as defined by the point spread function of the imaging system. The resulting image will be a superposition of each of these patterns. The contributing waves will each have its own amplitude, a_n, and phase, ϕ_n, at any given point in the image, (x,y). The resulting amplitude of the electric field at a given position is given by the complex sum of the amplitudes from each of the contributing point sources in the object

$$A(x,y) = \sum_{i=1}^{N} |a_n| e^{i\phi_n}. \tag{1.2}$$

If the sample is optically rough (as defined in Section 1.1), it can be assumed that the phases of the contributing waves are evenly distributed across the interval $[-\pi, \pi]$ [1]. This distribution of phases comes from the assumption that the path lengths traveled by each scattered photon is completely random on the scale of the optical wavelength [9]. This analysis of the amplitude of the electric field as a random phasor sum follows the same mathematical treatment of random walks. Such a random phasor sum follows a Rayleigh distribution as shown by

Goodman [10]. The probability distribution function (PDF) of the amplitude of the resulting field p_A is

$$p_A(A) = \frac{A}{{\sigma_a}^2} e^{\frac{-A^2}{2{\sigma_a}^2}} \tag{1.3}$$

where σ_a is a scale parameter that describes the width of the distribution.

This function describes the distribution of the amplitude of the field that makes up the speckle pattern. However, when speckle is imaged, the intensity of the field is measured. Therefore, the PDF of the intensity is of interest. Probability theory shows that the PDFs of two random variables, *u* and *z*, are related

$$p_z(z) = p_u(f^{-1}(z)) \left|\frac{du}{dz}\right| \tag{1.4}$$

where $u = f(z)$ [12].

The intensity, *I*, of polarized light is given by the absolute square of the field's amplitude. Hence, the intensity PDF of a polarized speckle pattern is given by a negative exponential

$$p_I(I) = \frac{1}{2{\sigma_a}^2} e^{\frac{-I}{2{\sigma_a}^2}} = \frac{1}{\langle I \rangle} e^{\frac{-I}{\langle I \rangle}}. \tag{1.5}$$

The right side of this equation uses the result that the mean intensity $<I>$ is $2\sigma_a^2$. The second moment and variance of the distribution are

$$\langle I^2 \rangle = \int_0^\infty I^2 p_I(I) dI = 2\langle I \rangle^2 \tag{1.6}$$

and

$${\sigma_I}^2 = \langle I^2 \rangle - \langle I \rangle^2 = \langle I \rangle^2. \tag{1.7}$$

Those far, two assumptions have been made in this model of speckle – (1) the phases of the contributing waves to the resulting superposition are uniformly distributed, and (2) the field is polarized. These assumptions define a *fully-developed* speckle pattern which has the characteristic property of having a contrast, as defined in Eqn. 1, equal to 1 [13]. This occurs because the standard deviation and mean are equal as seen in Eqn. 1.7.

If either of the two assumptions mentioned are not met, the speckle statistics change. If the speckle is *partially polarized*, the intensity is the sum of the intensities of the field amplitudes in two orthogonal directions. This leads to a change in the intensity PDF and ultimately a

decrease in the speckle contrast. When the underlying statistics of the phases, ϕ_n, are not uniformly distributed, the speckle is considered *partially developed*, and the contrast is reduced [10]. In experimental setups, there are always factors that will reduce the contrast of static speckle. Therefore, it is accepted that the contrast will follow the condition $0 \leq K \leq 1$ [8, 14, 15].

This is harmful to LSCI because it depends on temporal changes in speckle to reduce speckle contrast to sense flow. If the contrast of the speckle at any instant is already reduced by these underlying factors, LSCI's sensitivity is diminished. Khaksari and Kirkpatrick have recently published work that demonstrates the negative impact biased estimators of speckle statistics due to experimental parameters can have on LSCI [16].

1.3.2- Simulating Static Speckle

It has been shown that there is a simple method for simulating fully-developed speckle patterns [17]. This is accomplished by filling a circular region of a square matrix with complex values with equal amplitudes but with random phases between [-π π]. A two-dimensional spatial Fourier transform of this space will produce a pattern that follows the same statistics of the amplitude of the field that produces a fully-developed speckle pattern. The absolute square of the resulting matrix simulates the speckle intensity pattern. A MATLAB function to accomplish this procedure is provided in Appendix A.

Fig. 3 displays a sample of simulated speckle (Fig. 3a) and an experimentally captured speckle image (Fig. 3b) that have the same mean speckle size (speckle size is discussed in Section 2.2). The intensity distributions of these speckle patterns are shown in Fig. 4. The simulated speckle follows a negative exponential PDF. However, the experimentally imaged speckle deviates from the negative exponential. This deviation translates into a decrease in the speckle contrast of the images. The global contrast of the simulated speckle, found using Eqn. 1 for the entire image, is 0.98 while the experimental global contrast was 0.48. The slopes of the negative exponential distributions on the simulated and experimentally imaged speckle were also different for the intensities greater than the mean. An investigation of this deviation from the distribution's slope of the simulated speckle was not conducted. Obtaining a physical explanation of this change in the intensity distribution could be a future investigation.

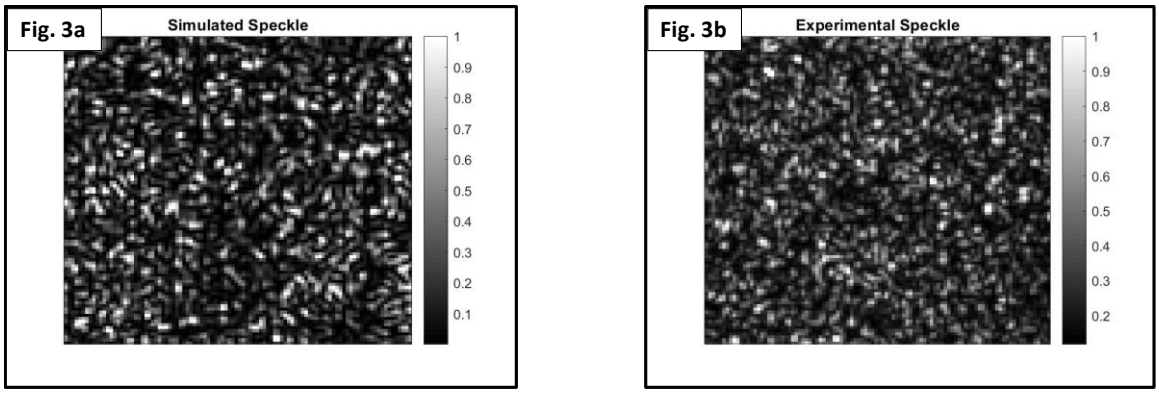

Figure 3. *The left figure (3a) shows a simulated speckle pattern created using the MATLAB function provided in Appendix A. The right figure (3b) provides an example of experimentally imaged speckle scattered from a plastic block. The speckle was imaged through a linear polarizer. The color bars show the intensity of the speckle normalized to the maximum intensity. The simulated speckle was constructed to have the sample pixel-to-speckle ratio as the experimental speckle (2.7 pixels/speckle).*

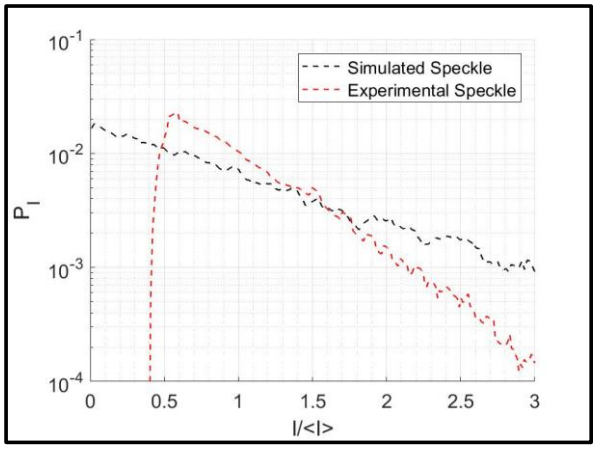

Figure 4. *The intensity PDF of the simulated speckle (black) follows the expected negative exponential form. The experimental speckle deviates from a negative exponential for intensities less than the mean (red).*

1.4- Relating Speckle Contrast to Flow

In the preceding section, the formation of the speckle is discussed. Now, the discussion is moved away from static speckle to provide the theory that allows laser speckle contrast imaging to be used to detect flow. For this to be accomplished, the relationship between the speckle contrast and flow rate of the particles must be described.

When scattering particles in an optically rough medium move, the intensity of the speckle that the reflected coherent light forms will fluctuate in time. These fluctuations ultimately depend

on the changing path lengths that the photons travel from the particles to the image plane. LSCI is dependent on capturing these fluctuations over the exposure time of the camera used to image the speckle. When the speckle fluctuates, the measured intensity of neighboring speckles in the image will blur together, and the contrast is reduced. LSCI uses this relationship to quantify and map flow of scattering media.

There is uncertainty in the exact relation between the particle flow rate and the measured speckle contrast, though there have been different models and schemes used in the field to relate the speckle contrast to the speed of the scattering particles [5, 18, 19]. These efforts of relating the flow speed and speckle contrast attempt to relate a decorrelation time, τ_c, of the field to the contrast. This decorrelation time is the decay time of the autocorrelation function the speckle's electrical field, g_1, and is assumed to be inversely proportional to the mean velocity, v, of the particles[4, 19, 20]

$$\tau_c \propto {}^{1}/_{v}. \tag{1.8}$$

In the development of LSCI, it has been common to assume the field's autocorrelation function has the form of a negative exponential [5]

$$g_1(\tau) = e^{-{}^{\tau}/_{\tau_c}}. \tag{1.9}$$

This comes from assuming a Lorentzian distribution of velocities of the scattering particles under Brownian motion [9, 15]. Table 1 provides the provides the PDF of a Lorentzian distribution.

Table 1. *Summary of the properties of Lorentzian and Gaussian distributions.*

Distribution	PDF	Mean	Median	Variance	FWHM
Lorentzian (a.k.a. Cauchy)	$\frac{1}{\pi\gamma\left[1+\left(\frac{x-x_o}{\gamma}\right)^2\right]}$	-	x_o	-	2γ
Gaussian (a.k.a. Normal)	$\frac{1}{\sqrt{2\pi\sigma^2}}e^{\frac{-(x-\mu)^2}{2\sigma^2}}$	μ	μ	σ^2	$2\sqrt{2\ln 2}\sigma$

Because photodetectors are sensitive to the intensity of light rather than the field itself, the Siegert relation must be used to relate the field's autocorrelation function to that of the intensity's autocorrelation function [20]

$$g_2(\tau) = 1 + \beta|g_1(\tau)|^2. \tag{1.10}$$

In this relation, β is a normalization factor that is dependent on various properties such as the polarization of the light and the ratio of the size of the detector to that of the speckle [4].

When speckle is imaged, the time-averaged intensity of the speckle pattern over the detector's exposure time, *T*, is obtained. The spatial variance of the imaged speckle is related to the autocovariance function, C_t, of the intensity fluctuations

$$\sigma^2(T) = \frac{\langle I\rangle^2}{T}\int_0^T C_t(\tau)\mathrm{d}\tau = \frac{\langle I\rangle^2\beta}{T}\int_0^T |g_1(\tau)|^2\mathrm{d}\tau. \tag{1.11}$$

By assuming β =1, Fercher and Briers were the first to use this model to create a relationship between speckle contrast, the correlation time and exposure time in 1981 as [5]

$$K = \frac{\sigma}{\langle I\rangle} = \left[\frac{\tau_c}{2T}\left\{1 - e^{-\frac{\tau_c}{2T}}\right\}\right]^{1/2}. \tag{1.12}$$

Others have constructed different models relating the correlation time to the speckle contrast [18, 19]. Several works have assumed a Gaussian distribution of flow velocities which changes the field's autocorrelations to

$$g_1(\tau) = e^{-(\tau/2\tau_c)^2} \tag{1.13}$$

and the derived contrast to [15, 21]

$$K = \frac{\sigma}{\langle I\rangle} = \left[\left(\frac{\pi}{4}\right)^{1/2}\left(\frac{\tau_c}{T}\right)\mathrm{erf}\left(\frac{\tau_c}{T}\right)\right]^{1/2}. \tag{1.14}$$

This velocity distribution is characteristic of ordered flow.

Khaksari and Kirkpatrick have shown that LSCI is sensitive to advective flux that models the motion of the scattering particles with diffusive motion plus a drift velocity [22]. This means that the motion of the particles is a sum of that due to thermal motion and directed or uniform flow. It has been shown that for the use of LSCI, the inverse decorrelation time can be sufficiently approximated to be proportional to the inverse of the squared contrast for both Lorentzian and Gaussian velocity distribution assumptions [15]

$$v \propto 1/\tau_c \propto \frac{1}{K^2}. \tag{1.15}$$

1.5- Applications, Limitations, and Techniques of LSCI

By measuring the contrast for each pixel within a speckle image, one can use the relations described here to generate a flow map of the sample with high temporal and spatial resolution [4]. The temporal resolution is only limited by the exposure time used to capture the images, and the spatial resolution is dependent on the resolution of the imaging optics. This has allowed LSCI to be implemented in a wide range of applications, specifically biomedical applications.

LSCI has been used to sense and quantify blood perfusion in many applications in the human body [4, 6, 8, 23-29]. In such applications, it is assumed that the red blood cells in the tissue's vasculature are the primary scattering particles [8]. Speckle contrast was first used by Fercher and Briers in 1981 to visualize blood flow in the retina [30]. Since, it has been used in many applications from assessing microvascular perfusion in skin [23, 24] to mapping cerebral blood flow [31, 32]. It has also been demonstrated that LSCI can be implemented inexpensively [33] and can have high reproducibility in flow measurements [24]. Being able to provide wide-field maps of flow with high temporal and spatial resolution without requiring expensive setups makes LSCI an advantageous technique compared to other commonly adopted optical, flow-monitoring techniques such as laser doppler flowmetry (LDF) [34] and diffuse correlation spectroscopy (DCS)[35].

There are limitations to the implementation of LSCI. The first limitation is difficult to measure absolute flow rates when compared with LDF or DCS[4, 21]. This means that LSCI is only able to detect relative changes in flow rates. It has also been shown that the scattering and absorptive properties effect LSCI measurements [36] and only superficial flow in tissue can be sensed [37]. Many studies have also shown that the presence of static scatterers have detrimental effects to LSCI [4, 7]. Even with these limitations, work is being done to improve the use of LSCI.

Many variations of using laser speckle contrast to detect flow have been developed. Fercher and Briers first used long, single-exposure photography to analyze the blurring of speckle [5]. A digital version of single-exposure speckle photography was established by Briers in 1995 [38]. Then, laser speckle contrast analysis (LASCA) was developed in 1996 in which the spatial speckle contrast was used to map capillary blood flow in the hand [6]. The technique described in this work is the basis of the speckle contrast imaging described in this work. This technique is commonly referred as spatial laser speckle contrast imaging because it uses the spatial standard deviation and mean of intensity about each pixel used to image the speckle to quantify the contrast. The intensity measurements of pixels within a 5x5 or 7x7 pixel region are typically used to calculate the local speckle contrast for each pixel. A temporal version of this analysis in which contrast for each pixel is found using a temporal stack of speckle images has been used to increase spatial resolution of LSCI. It has been demonstrated that this technique decreases the detrimental effects of scatterers to LSCI's ability to sense flow [39]. More recently, many variations of LSCI have been developed including multi-exposure LSCI and spatial frequency domain LSCI [19, 40].

1.6- Objectives

The focus of this thesis is to present the progress that has been made toward establishing laser speckle contrasting imaging as a flow-imaging technique and toward understanding the technique's sensitivity to buried flow in optical phantoms. Specifically, results of experimental investigations of single-exposure, spatial LSCI were examined. It's first demonstrated that my LSCI setup is capable of sensing changes in blood flow *in vivo*. Then, the technique's sensitivity to buried flow in optical phantoms is examined. The goal is to investigate the effects of illumination wavelength and polarization on LSCI's depth-sensitivity to flow.

Chapter 2– Experimental Approach

2.1- Imaging Setup

There are three components to a laser speckle contrast imaging setup- (1) a coherent light source, (2) optics to uniformly illuminate the sample, and (3) a camera to image the light backscattered from the sample of interest. Fig. 5 shows a schematic of the typical LSCI setup. In this section, I present a general description of the setups used to conduct the experiments described in the following chapters. Details of the specific instrumentation and acquisition parameters are provided in the corresponding chapters.

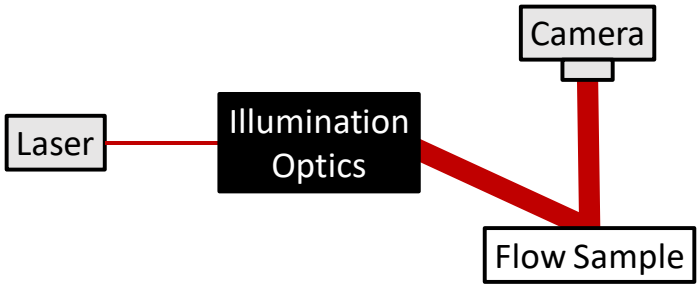

Figure 5. *A schematic of a typical LSCI setup including a coherent source, illumination optics, and a digital camera.*

2.1.1- Illumination Setup

In the experiments described below, four different lasers were used. The wavelengths of the sources varied and are outlined in Table 1. Mirrors were used to direct the beams from each of these sources to pass through a ground-glass diffuser (DG10-1500-MD; Thorlabs, Inc.) to provide an even illumination of the flow samples (Fig. 10). In addition to the ground glass diffuser, a beam expander constructed from free lenses was used following the diffuser in the experiments conducted to investigate the effect of polarization on LSCI's depth-sensitivity (Fig. 16). The mirrors were positioned so that the beam from a mounted source was directed toward the ROI of the sample at an angle to minimize specular reflections from reaching the camera used to image the scattered light. Specular reflections are those that reflect from the surface of the flow sample rather than the scattering particles embedded in the fluid. This means that the specular reflections do not contain information about the flow rate of the medium and should be avoided. Neutral density filters were used if necessary to avoid saturation of the detector which can be detrimental to LSCI [16]. The filters were mounted in the path of the illuminating light. The speckle intensity should be distributed within the dynamic range of the camera being used to image the sample so that all speckle fluctuations can be sensed by the photodetectors.

Table 2. *Description of the coherent sources used to illuminate flow samples*

Wavelength	Description	Manufacture (Product #)
785 nm	Stabilized laser diode	Innovative Photonics Solutions, NJ (I0785SH0100B-TH-L)
633 nm	HeNe laser	Melles Griot; USA
532 nm	Laser diode	Aixiz.com (AD-532-25ADJ)
405nm	Laser diode	Aixiz.com ((AH405-201230)

2.1.2- Imaging Setup

A CMOS digital camera (SME-B012-U; Mightex Systems, Pleasanton, CA) was used to image the speckle scattered from the flow samples. The camera had a 1280x960 array of pixels with a single pixel area of 14 μm^2 and an 8-bit depth. A focusing lens with a variable aperture was used to focus the camera on the sample. The focal length and aperture size used for each experiment are provided below. In each setup, the camera was positioned such that the imaging axis was normal to the surface of the flow sample to avoid specular reflections. If the flow sample was a tube, the tube was positioned such that the axis of the tube ran parallel to one of the edges of the captured image. This allowed a rectangular ROI within the tube (as described in Section 2.3) to be easily indexed using MATLAB during the computational analysis.

The software provided from the manufacture was used to control the imaging parameters including the exposure time, frame rate, and image resolution. The IR filter that was mounted in front of the detector was removed when the 785nm source was used. The software saved each captured frame as a bitmap image to the controlling computer. Appendix D provides a description of how to control the camera and its settings.

2.2- Imaging Parameters

In this section, I provide a description of three imaging parameters that must be considered to successfully conduct LSCI. These include the uniformity of the illumination, exposure time of the camera, and the size of the speckle.

2.2.1- Uniform Sample Illumination

It is important to have an evenly illuminated region of interest (ROI) with LSCI. This was accomplished here with the use of a diffuser in the path of the illumination. It is important to have a constant mean intensity in the speckle image because the speckle contrast is dependent on the mean intensity (Eqn. 1).

In preliminary work of this thesis, three factors that lead to uneven illumination were avoided in the experimental setups of this work. The first was the presence of shadows in the speckle images. A tube was used in the flow phantoms for these experiments. Such a tube could

cause shadows in the images if positioned to run perpendicularly to the axis of the illumination as demonstrated in Fig. 6a. If the contrast outside of the tube is of interest, the shadows cast by the tube must be avoided. These shadows were prevented by positioning the tube parallel with the axis of illumination such that the areas beside of the tube were uniformly illuminated.

The second cause of nonuniform illumination that was noticed when the illumination was passed through a multi-mode optical fiber. A mode describes the optical path that light travels down the fiber. In multi-mode fibers, it is possible for light to take different paths from one end of the fiber to the other. This means that the different modes could be out of phase when leaving the fiber. Interference of the various modes leaving the fiber caused the intensity of the illumination to be nonuniform as shown in Fig. 6a. This was corrected in the presented experiments by using free optics and a diffuser to illuminate the samples.

The final source of nonuniform illumination was noticed when the beam from the 785 nm source was expanded using a beam expander (described in Section 5.2.1). The source did not have a Gaussian intensity pattern, Fig. 6b. This was corrected by positioning a ground-glass diffuser (DG10-1500-MD; Thorlabs, Inc.) before the expander.

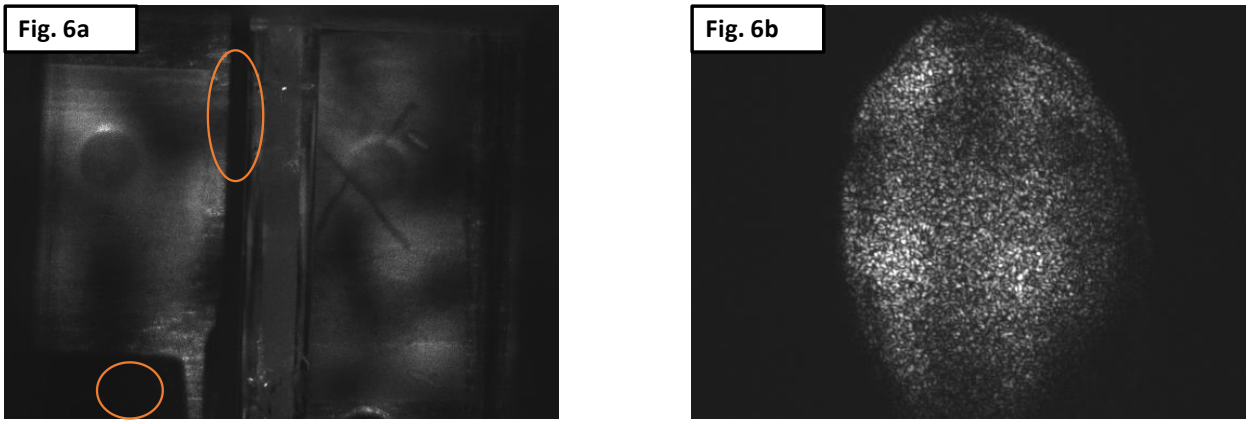

Figure 6. *This figure shows speckle images that were captured with nonuniform illumination. Fig. 6a was illuminated through a multimode optical fiber. The interference from the various modes can be observed throughout the image. In addition, shadows (such as those partially highlighted by orange circles) can be seen. In Fig. 6b, the nonuniform illumination caused by the transverse modes of the source was observed when the 785 nm beam was expanded with a beam expander.*

2.2.2- Exposure Time

The spatial variance of imaged speckle is the time average of the autocovariance of the intensity signal over the exposure time (Eqn. 1.11). Therefore, LSCI is dependent on the exposure time used to capture speckle images. Specifically, the speckle contrast is dependent on the ratio of the speckle decorrelation time and exposure time (Eqn. 1.12 or 1.14). Previous work has investigated

the noise and sensitivity in LSCI for detecting flow changes associated with the exposure time [41]. Commonly used exposure times with LSCI (6 ms and 10 ms) for biomedical applications were used in these studies [4]. In preliminary studies, it was observed that the sensitivity of LSCI measurements to increasing flow rates decreased as the flow rate increased. In addition, it was found that this relationship between LSCI's ability to distinguish between flow rates is dependent on the exposure time used to image the speckle. For higher flow rates, a shorter exposure time is required to be able to differentiate between flow rates. This dependence is why the flow rates in the study discussed in Chapter 6 were significantly decreased compared the rates used in the study described in Chapter 5.

2.2.3- Speckle Size

With LSCI, the photodetectors within the imaging array are used to spatially sample the speckle. Therefore, the ratio between the size of the pixels to the size of the speckle must be considered when imaging the speckle [42]. The minimal ratio to meet the Nyquist theorem is 2. With this pixel-to-speckle ratio, it is assumed that the intensity measurements spatially sample the speckle intensity at a higher frequency than the highest spatial frequency present in the speckle pattern. Thus, it is ensured that a single pixel is not sensing the intensity of multiple speckles and aliasing the real spatial frequency of the speckle.

The size of the speckles in an image is dependent upon the wavelength of light used to illuminate the sample, λ, and the optics used to image the sample (specifically, the size of the aperture through which the sample is imaged, *f/#*, and the magnification of the lens, *M*). In many studies, the minimum size of speckle is estimated by [4, 42]

$$\rho_{speckle} = 2.44\lambda(1 + M)\,{}^{f}\!/_{\#}. \tag{2.1}$$

Since this equation approximates the size of the speckle, it is beneficial to be able to experimentally calculate the size of the speckle in captured images. This can be done by calculating the full width at half max (FWHM) of the spatial autocovariance function or power spectral density of intensity in a speckle image [43, 44]. A MATLAB function (see Appendix B) was created to calculate the FWHM of the spatial autocovariance to provide an experimental estimation of the average speckle size of an image as demonstrated in Fig. 7a. The function first spatially convolves the speckle image with itself. It then fits the middle 7 lag steps (-3 to 3 pixels) to a Gaussian curve. The fit parameters are then used to estimate the FWHM of the autocovariance curve of the speckle image. The function repeats this analysis in both the horizontal and vertical directions of the 2D speckle image. The horizontal autocovariance is obtained by offsetting the image horizontally with itself for a range of lags equal to twice the number of columns in the image plus one in units of pixels. The range of the vertical lags is equal to twice the number of rows in the image plus one. This allows the function to estimate the speckle size in both the vertical and horizontal directions. With this code, it was ensured that the captured images were sufficiently sampled. Fig. 7b provides a plot of the experimental

estimation and theoretical estimation (Eqn. 2.1) of the speckle size as a function of aperture size for three f/#'s (4, 8 and 16). It was observed that the experimental speckle sizes as a function of aperture size had a smaller slope than the theoretical estimation. This suggests that the aperture size influences the size of the speckle in experimental setups to a lesser manner than given by Eqn. 2.1.

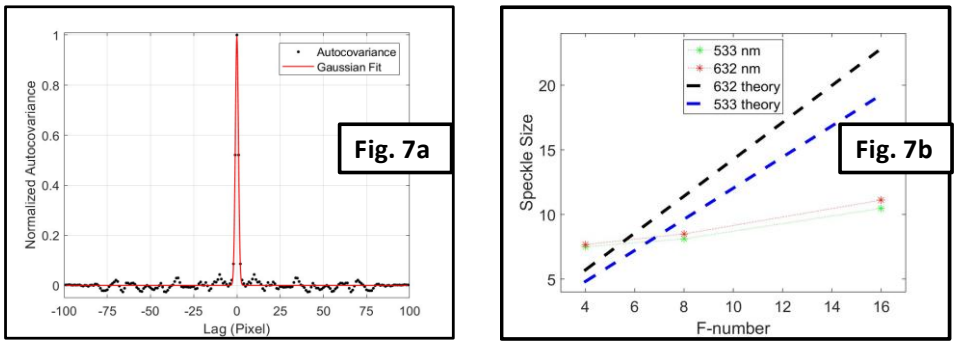

Figure 7. *This figure is the normalized spatial autocovariance function of the static speckle image shown in Fig. 3b (Fig. 7a). The FWHM of the curve is an empirical estimation of the average speckle size (2.65 pixels here). Fig. 7b compares the size of the speckle estimated by Equation 2.1 (dashed lines) to the speckle size calculated from the FWHM of the autocovariance function of raw speckle images captured at three aperture sizes for two wavelengths [632nm (red stars/black line) and 533 nm (green stars/blue line)].*

2.3- Computational Processing

LSCI requires post-processing of the captured speckle intensity images to calculate the speckle contrast and provide a flow index of the scattering medium. MATLAB was the programming platform that was selected to compete the laser speckle contrast analysis (LASCA) for this thesis.

The bitmap files of the capture speckle images were uploaded into the MATLAB workspace as two-dimensional matrices. The local speckle contrast (Eqn. 1) was calculated from a 7x7 region of pixels surrounding each pixel in the image, creating a contrast map of the sample. The contrast at each pixel was then fit to either Eqn. 1.12 or Eqn 1.14 to provide a flow index. To provide a single measured flow rate of the sample for each captured image, the mean flow index value was found within a rectangular ROI.

MATLAB functions used to compute the contrast maps are provided in Appendix C. A significant amount of work that lead to the completion of this thesis was directed to optimizing the computational tools needed to conduct LSCI experiments. Many speckle images are captured in each of the experiments described in this thesis. Therefore, it was important to create a

MATLAB function that calculated the speckle contrast of an image as fast as possible. Two different functions are presented to demonstrate the progress that was made to improve the speed of the analysis during the completion of this thesis. Appendix C.1 provides the first version of the LASCA function that was used. In this function, the contrast is found for each pixel by looping through the indices of each pixel in the 2-D array of intensity values. This function was replaced by the function provided in Appendix C.2. The updated function avoids looping through the indices of each pixel and computes the contrast using element-by-element computations. This increased the rate at which contrast maps can be generated. The original function takes 160 ms to compute the contrast map for a 100x100 pixels speckle image compared to the 15 ms that it takes the updated function to compute the same contrast map.

Chapter 3– Quantifying Post-Occlusive Reactive Hyperemia

3.1- Introduction

The purpose of Chapter 3 is to provide a validation of our LSCI's ability to sense *in-vivo* changes of blood flow. The chapter outlines the work that was presented at the 2016 SPIE Photonics West conference. A complete description of the study titled *Quantitative assessment of reactive hyperemia using laser speckle contrast imaging at multiple wavelength* is provided in the conference proceedings [26].

Post occlusive reactive hyperemia (PORH) describes an increase in blood flow within tissue following the release of a local occlusion. This physiological response can be used as a health indicator for various medical conditions including atherosclerosis, age, and hypertension and could predict cardiovascular risks [45-48]. This response was chosen to be studied for this study because it can be readily induced in subject's and has been assessed with LSCI by others [24, 27, 29]. The primary goals of the study presented here were to assess the utility of LSCI to quantitatively evaluate PORH and examine the impact of using light sources at different wavelengths.

3.2- Methods

Blood perfusion in the forearms of 3 healthy, young adult volunteer subjects (aged between 20-21 years) was measured with LSCI before, during, and after a 60-second occlusion was applied to their upper arm at pressures greater than their systolic blood pressure with a standard blood pressure cuff [26]. Free optics were used to direct the beam from the illuminating source through an expanding lens and optical diffuser to evenly illuminate a 20 cm^2 area on the ventral side of their forearm.

Beginning 30 seconds before the application of the occlusion, the camera captured 650 raw speckle images with an exposure time of 10 ms at a rate of 4.3 Hz. The aperture of the camera was set to have a f-number of 4. This process was repeated for each subject for the 633 nm, 532 nm, and 405 nm sources described in Table 1. Between each PORH test using different wavelengths, the subjects were given time to rest to allow for the blood flow in their arms to completely recover to baseline values.

LSCI analysis was performed over an ROI of 800 × 700 pixels for each of the raw speckle images acquired. A LSCI flow index for each image was calculated using the mean of the inverse of the contrast squared (Eqn. 1.15) within the selected ROI. Calculating this flow index for each image provided a time sequence of blood perfusion measurements.

3.3- Results and Discussion

Fig. 8 shows the results of a PORH test obtained from the subjects for all three wavelengths. The results of the 633 nm and 532 nm wavelength trial produced expected results in patterns of reactive hyperemia. The flow measurements quickly peaked above the baseline flow following the release of the pressure. However, the results obtained using the 405 nm wavelength showed a much different time-course. These blood flow measurements decreased following the release of the occlusion before returning to baseline.

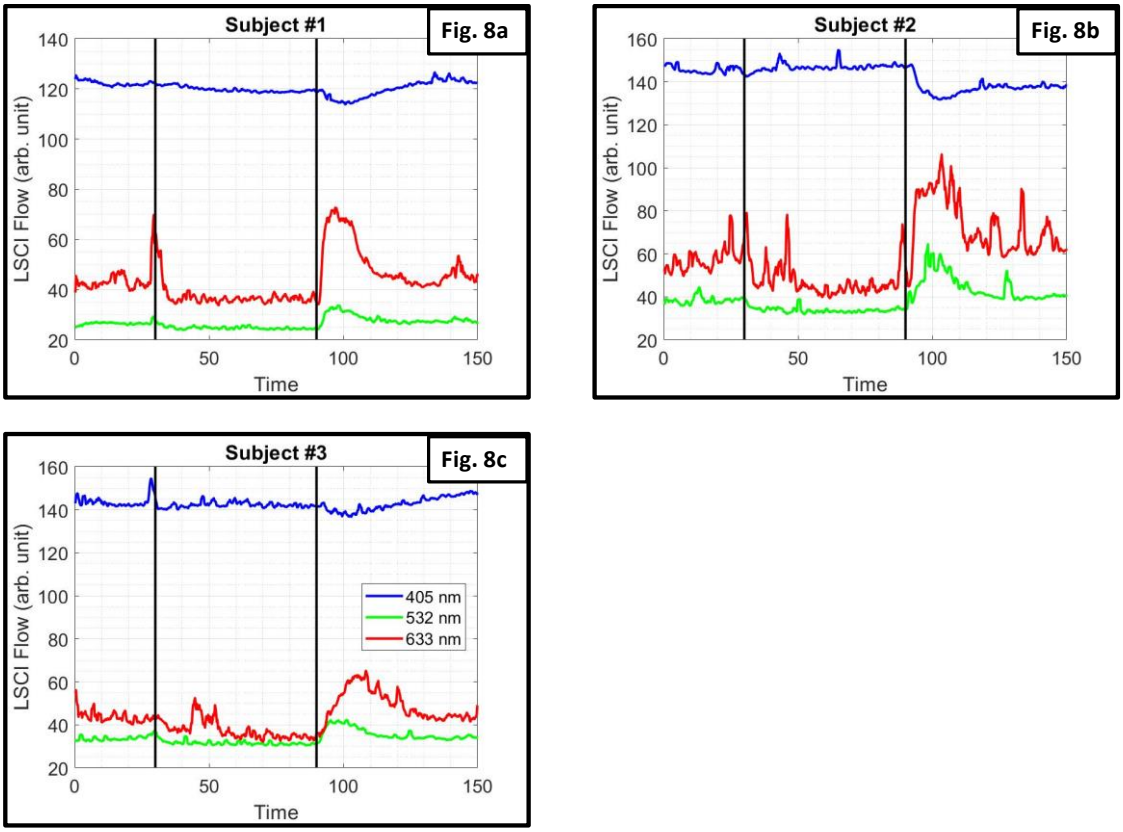

Figure 8. *These figures show the repeated LSCI flow measurements while conducting a PORH test for all three subjects. The three plots on each figure correspond to the three wavelengths used in the study- 405 nm (blue), 533 nm (green), and 633 nm (red). The vertical lines approximate when the occlusion was applied and released. Note the decrease in flow measurements following the occlusion release while using the 405 nm and the sharp increase for the 533 nm and 633 nm sources.*

The results of this study demonstrated that our LSCI setup could sense and quantify induced changes in blood perfusion *in-vivo* in highly scattering tissue demonstrated in the skin of the forearms. They also indicated that the LSCI measurements were dependent on the illumination wavelength. One explanation for the wavelength dependence could be the wavelength-dependent nature of the scattering and absorptive properties of the tissue. Varying

the optical properties of the flowing media is known to change LSCI flow measurements for a single illumination wavelength [36]. Therefore, it would be expected that induced changes in optical properties caused by varying the wavelengths would also affect the LSCI measurements.

This investigation raised the question whether the wavelength of light affected the depth of the microvasculature of which LSCI was detecting the flow. For example, could a longer wavelength, which is known to penetrate tissue deeper, be experimentally chosen if the flow rates of deeper vasculature were of interest. On the contrary, could a shorter wavelength, which would be assumed to be scattered more from superficial vasculature, be used to selectively sense flow through microvasculature in the most superficial tissue? Such inquiries lead to the completion of experiments to investigate the depth-sensitivity of LSCI using flow phantoms in which the optical properties of the samples and depth of flow could be controlled.

Chapter 4– Investigating the Sensitivity of LSCI to Buried Flow

4.1- Introduction

The objective of this work presented in this chapter was to experimentally investigate spatial LSCI's sensitivity to flow through a channel embedded within an optical phantom of slow-moving scatterers (i.e. only thermal motion present). Two separate experiments were conducted in this study. The first investigated the sensitivity as a function of the depth at which the channel was buried for a constant surrounding media. The second examined the effects the optical properties of the surrounding media had on LSCI's depth-sensitivity as the scattering and absorption properties of the surrounding media were varied. These experiments were completed with 633 nm and 785 nm illumination (see Table 1 for details) to examine the wavelength-dependence of the flow sensitivity through scattering media. The goal of the work presented in this chapter is to experimentally investigate the depth-sensitivity of LSCI for detecting fluid flow embedded in controlled turbid optical phantoms.

4.2- Methods

LSCI was used to measure flow through a flow channel embedded in a turbid medium to assess the effect that the buried depth of the channel and the optical properties of the media surrounding the channel had on LSCI's ability to sense flow. The setup used in this study allowed for control of both the optical properties and depth of the flow phantom.

To construct the flow phantom for this study, a clear, plastic tube (inner diameter (ID): 1.6 mm; outer diameter (OD) = 3.2 mm) was fixed to the bottom surface of a rectangular chamber (6.5 cm x 6.5 cm x 1.0 cm tall) to function as a flow channel. Fig. 9 shows an image of the setup and phantom used in this study. A syringe pump (75900-00; Cole-Parmer Instruments Co., Vernon Hills, IL) was used to flow a solution of 1 μm-diameter polystyrene microspheres (Polybead microspheres, 07310, Polysciences Inc., Warrington, PA) [49, 50]in water through the channel at 0, 3, and 6 mL/min for each of the experimental setups described below. For all experiments, the flowing medium had a reduced scattering coefficient, μ_s', of 24 cm^{-1} at 785 nm (27 cm^{-1} at 633 nm) as calculated using Mie theory [51] and a negligible absorption coefficient, μ_a.

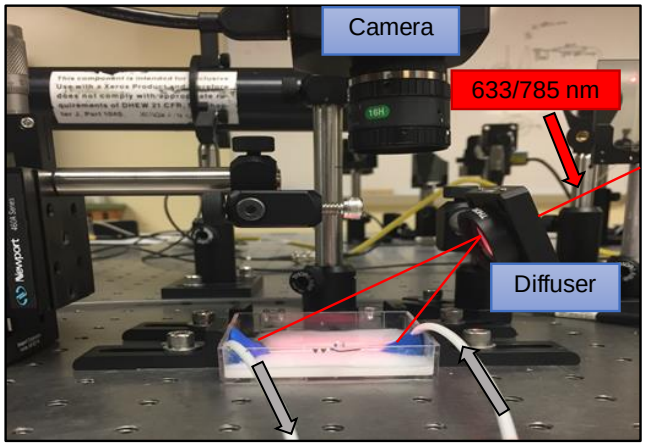

Figure 9. *An image of the flow phantom and imaging setup used in the depth-sensitivity study. The grey arrows in the figure indicate the direction of flow from a syringe pump to a sink. LSCI images were captured with a CMOS camera using one illumination wavelength at a time while the other source was blocked. The beams were expanded using a ground glass diffuser to illuminate the phantom, and the intensity of the beam were controlled using neutral density filters.*

For the first set of experiments, the buried depth of the channel, *d*, was varied by adding constant volumes of a surrounding fluid to the chamber. The fluid added to the chamber was composed of a solution of 1 μm-diameter polystyrene microspheres with a μ_s' of 6 cm^{-1} at 785 nm (7 cm^{-1} at 633 nm) with negligible absorbance [49, 50]. The depth of the channel from the surface of the surrounding media was increased from a baseline depth (at which the tube was just covered) in increments of 0.3 mm to a maximum of 2.4 mm (these nine phantoms are referred to as D1 (d=0 mm) through D9 (d=2.4 mm).).

To investigate the effect that the optical properties had on the LSCI flow measurements, the chamber was filled to a fixed depth of 600 μm while the optical properties of the surrounding were varied. Four combinations of scattering and absorption coefficients were used as displayed in Table 2. The absorption coefficient was controlled by dissolving Bovine Hemoglobin (H3760; MilliporeSigma, MO) in the polystyrene solutions [49, 50]. The absorption coefficients were determined from the measured absorbance of a stock solution of the hemoglobin with a spectrophotometer (Cary 100 UV-Vis, Agilent Technologies, Wilmington, DE).

***Table 3**. Description of the optical properties of the surrounding medium.*

Phantom ID	Absorption Coefficient (cm^{-1})		Reduced Scattering Coefficient (cm^{-1})	
	633 nm	785 nm	633 nm	785 nm
P1	0.10	0.02	3.4	3.0
P2	0.39	0.08	3.4	3.0
P3	0.10	0.02	6.7	6.0
P4	0.39	0.08	6.7	6.0

Only one source (either 633 nm or 785 nm) illuminated the sample at a time. A series of mirrors mounted on flip-mounts was used to control which source illuminated the sample as shown in Fig. 10. The other beam was blocked using absorbing beam blocks. Neutral density filters were place in the optical paths of the beams to prevent saturation of the camera imaging the samples. A ground-glass diffuser was used to evenly illuminate flow samples over a ~6 cm-diameter area with an average power of 0.20 mW and 0.38 mW of power at 633 nm and 785 nm, respectively, at the surface of the phantom. The backscattered images were captured using the Mightex Camera described in Section 2.1.2. The camera was focused to the phantom's surface using a focusing lens (f/8, focal length 8 mm). All speckle images were collected with an exposure time of 10 ms. The pixel-to-speckle ratios were measured to be 2.6 and 3.0 for the 632 nm and 785 nm sources respectively with the MATLAB function described in Section 2.2.3 (Appendix B), satisfying the Nyquist Theorem [42]. For each sample in both sets of experiments, 15 speckle images were captured at 100 Hz for all three flow rates (0, 3, and 6 mL/min).

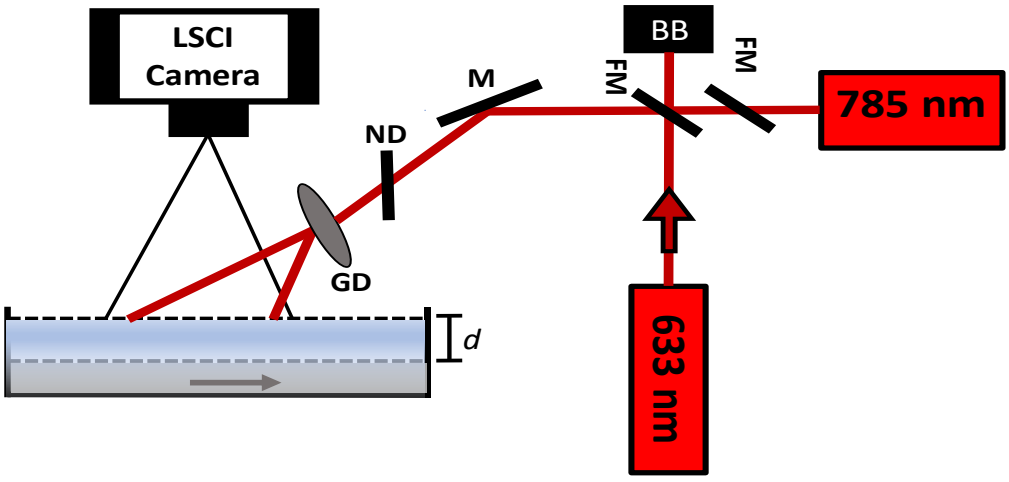

***Figure 10.** Schematic of the imaging system used to collect speckle images. Flip mirrors were used to select the illumination source. FM: Flip mirror; BB: Beam block; M: Mirror; ND: Neutral density filter; GD: Ground-glass diffuser; d: channel depth*

The MATLAB function provided in Appendix C.2 was used to find the speckle contrast for the pixels within a 100x10 pixel ROI selected directly atop the flow channel in each image as indicated in Fig. 10. The values were fit to Eqn. 1.12 using T = 10 ms, to find the inverse decorrelation time ($1/\tau_c$) for each pixel. The LSCI flow index, F_{LSCI}, for each image was taken to be the mean inverse decorrelation time within the selected ROI for each image. The error associated with each measurement was taken to be the standard deviation of F_{LSCI} across the 15 repeated images. To compare the relative changes in the flow measurements, all LSCI flow indices were normalized by the flow index derived from the phantom used in the depth study at d = 0.0 mm.

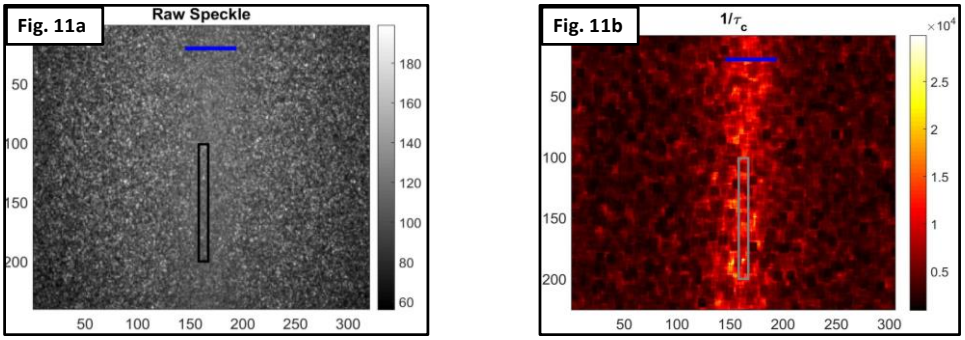

Figure 11. *The raw speckle image (Fig. 11a) and the LSCI flow map of τc^{-1} (Fig. 11b) computed using Eq. (1). Horizontal blue lines indicate the inner diameter of the flow channel and black (or gray) boxes the ROI used to compute average LSCI flow value. Images show data for one LSCI image at 785 nm illumination for at the baseline depth, at a flow rate of 6ml/min.*

4.3- Results and Discussion

Fig. 12 shows a panel of representative LSCI flow images obtained for the phantoms D1, D3 and D5 (rows) at flow speeds of 0 mL/min (left column) and 6 ml/min (right column). Visually, it is easy to perceive the demarcation of the flow channel for the flow speed of 6 mL/min relative to no flow (top row) for shallow depths, but the ability to do so decreases as the flow is buried under the scattering media.

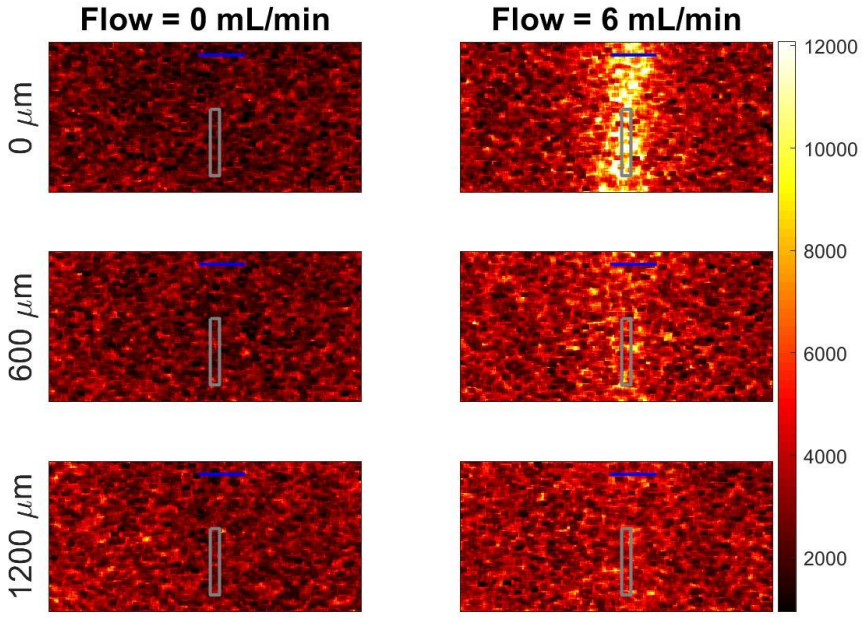

Figure 12. *Panel of representative LSCI contrast images obtained with the 785 nm source as the depth of the flow channel was varied shown for D1, D5 and D10 phantoms at two pump flow speeds. The blue bar indicates the flow channel's outer diameter while the grey boxes show the ROIs used for quantifying these data.*

The normalized F_{LSCI} data for all the phantoms D1-D9, for both illumination sources (Fig. 13a: 633 nm illumination, Fig. 13b: 785 nm illumination) are plotted as a function of depth in Fig. 12. The normalization values (the mean F_{LSCI} from the D1 phantom) were 6.85 x 10^3 s^{-1} and 2.27 x 10^3 s^{-1} for the 633 nm and 785 nm data respectively. LSCI measurements distinguished 0 mL/min flow from both the 3 mL/min and 6 mL/min flow, but it was not possible to correctly distinguish the two flow speeds.

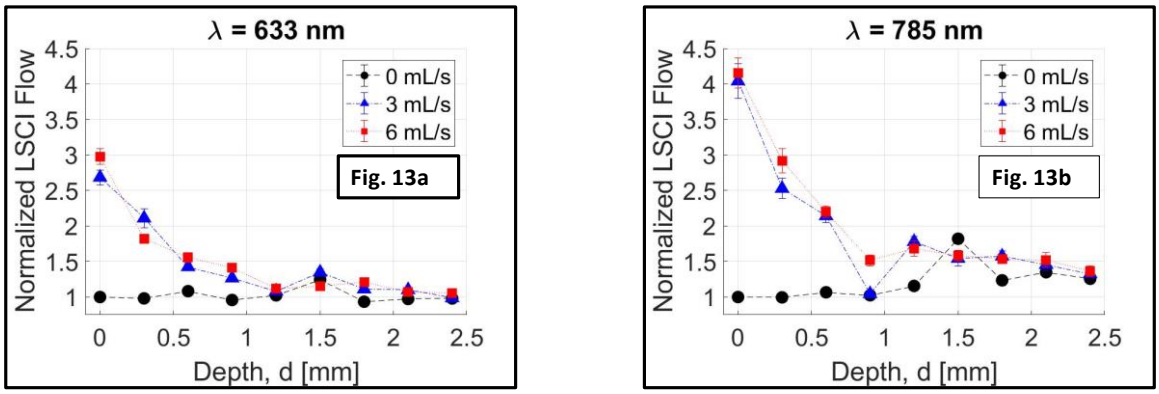

Figure 13. *LSCI data for the data collected using the 633 nm (Fig. 13a) and 785 nm (Fig. 13b) sources for all three flow rates (see legend) normalized to the corresponding wavelength's measurement of the D1 phantom with zero flow.*

The normalized flow indices for the four phantoms that possessed different optical properties of the surrounding media (P1-P4) are displayed in Fig. 14. The data shows that the normalized LSCI flow parameter at 785 nm was in general more sensitive and was on average nearly 1.60 times greater than the corresponding 633 nm values. It is also seen that for both wavelengths and both flow rates, the normalized LSCI flow sensitivity was greatest for phantom P1 – which was the phantom with the lowest scattering and absorption coefficients (see Table 2). The mean, normalized LSCI flow index for all phantoms and wavelengths was higher for 6 mL/min than 3 mL/min except for P4 with 785 nm illumination.

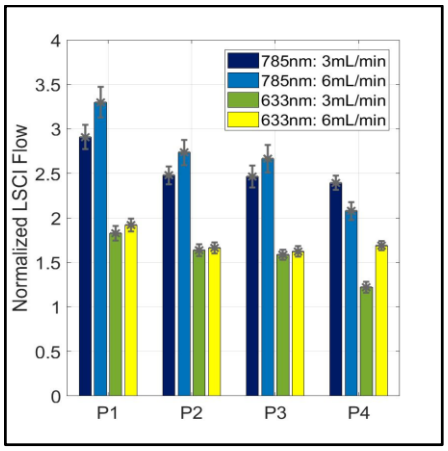

Figure 14. *LSCI normalized flow indices for the nonzero flow rates in each optical phantom outlined in Table 1. Two illumination wavelengths (785 nm and 633 nm) were separately used to collect LSCI experimental data was used to collect data for each phantom and flow rate at a fixed 600 μm depth.*

The results obtained during this investigation indicate that differences in optical properties of an optically turbid medium, and the depth of the embedded flow-channel both impact flow parameters derived from LSCI measurements. As the depth of the flow increased, the LSCI measurements of the flow through the buried channel decreased for both illuminations. These results agree with previous studies that have shown that increasing the amount of static scattering above a flow sample diminishes LSCI ability to sense the flow beneath [19, 42]. This investigation also demonstrated that the 785 nm illuminate provided greater sensitivity to the buried flow at all depths, suggesting that the wavelength of light should be considered when applying LSCI to detect buried flow [52]. The results from the phantoms with varying optical properties also show that the 785 nm was more sensitive to the buried flow. Both illuminations were negatively impacted by an increase in either the scattering or absorption coefficients of the surrounding media.

The experimental investigation described in this chapter have demonstrated that LSCI is sensitive to more than just the flow rate of the scattering particles. The results demonstrate that LSCI is sensitive to the optical properties of media surrounding the flow through which the light is scattered which is in turn dependent on the wavelength of light that is scattered. In general, this displays a difficulty that prohibits from being able to practically assess the absolute flow in biomedical tissue. The work described here suggests the measurements would have to be calibrated to the optical properties of the tissue in which the vasculature of interest is embedded in.

Chapter 5– Polarized Laser Speckle Contrast Imaging

5.1- Introduction

In Section 1.3.1, it is mentioned that having a field that is *partially polarized* changes the underlying statics of speckle and decreases the maximum speckle contrast. In LSCI, this parameter leads to a change in the statistics of the temporally integrated speckle that is imaged (See Goodman, Section 4.6.4) [9]. In this chapter, I present an experimental investigation of the effect that the state and direction of polarization relative to that of a linearly polarized illumination source has on LSCI's sensitivity to flow through a buried channel like the one described in Chapter 4. The data presented those far in this thesis have all examine the LSCI measurements obtained from the scattered field at all polarization states.

Polarizing filters have been commonly used with laser speckle imaging techniques to limit the amount of specular reflections that reaches the imaging plane because surface reflections would be highly polarized [53]. The more polarized light is multiply scattered, the light will become less polarized. Light that experiences many scattering events should contain photons that are polarized perpendicular to the illuminating light than light that has been singly scattered. This means that the polarization of light back-scattered from a turbid media should be less polarized compared to the illuminating source as it is scattered from deeper in the media. Therefore, it could be expected that LSCI's sensitivity to buried flow could be increased by selecting for photons with cross polarization. The study outlined here seeks to address this hypothesis.

5.2- Methods

5.2.1- Optical Setup

LSCI measurements were obtained by using a 785 nm laser source (See Table 1) to illuminate the flow phantoms. The optical path of the beam passed through a ground glass diffuser followed two beam expanders consisting of lenses with 19 mm, 50.2 mm, 25.4mm and 100 mm focal lengths. To construct the beam expanders, the two lenses were positioned such that the distance between them was equal to the sum of their focal lengths as demonstrated in Fig. 15. The light then passed through a neutral density filter and linear polarizer (LPNIRE100-B; Thorlabs, NJ) before being directed with a mirror to illuminate a roughly 2 cm diameter area of the phantom.

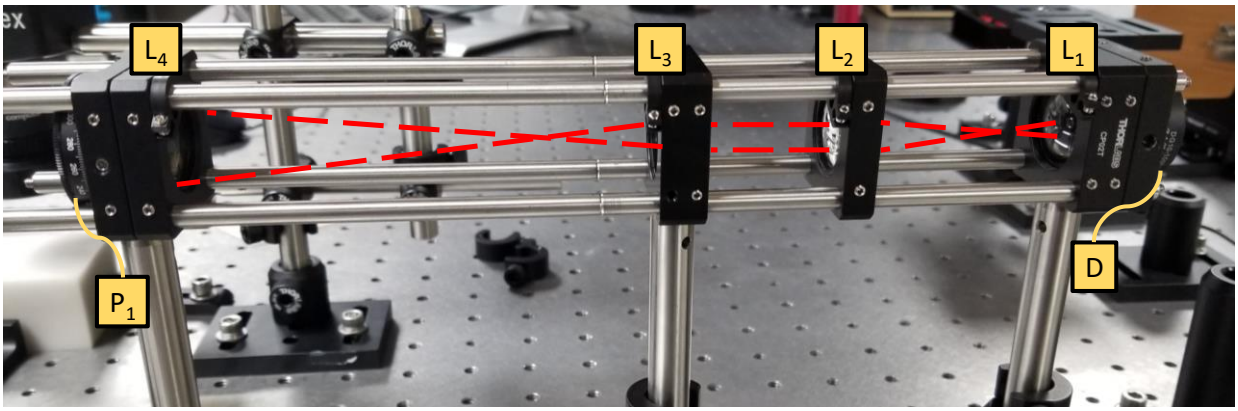

Figure 15. *This image shows the two beam expanders used in the polarized LSCI setup the is shown in Fig. 16. The ground-glass diffuser, four lens, and polarizer were mounted to a 30 mm optical cage system (Thorlabs, Inc.). The red, dashed lines represent a ray diagram through the expanders. D: Ground diffuser; L_1: 19 mm lens; L_2: 50.2 mm lens; L_3: 25.4 mm lens; L_4: 100 mm lens; P_1: Polarizer.*

Fig. 16 provides an image and schematic of the optical setup used in this study. This first polarizer was used to ensure that the incident illumination was completely polarized. The backscattered images were captured with the Mightex camera described in Section 2.1.2. The camera was focused on the flow channel using a focusing lens (f/8, focal length 8 mm). The pixel-to-speckle sizes were estimated to be 2.7 using the analysis outlined in Section 2.2.3.

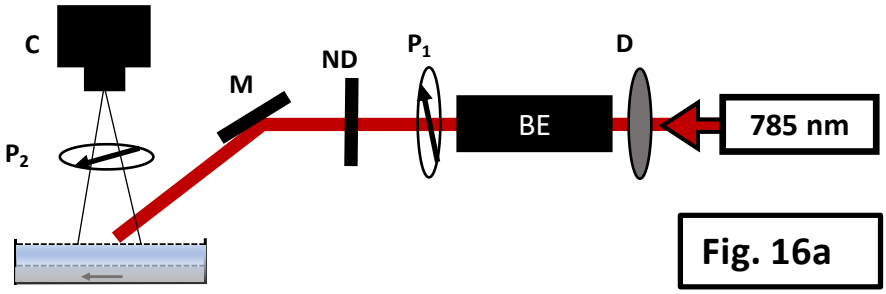

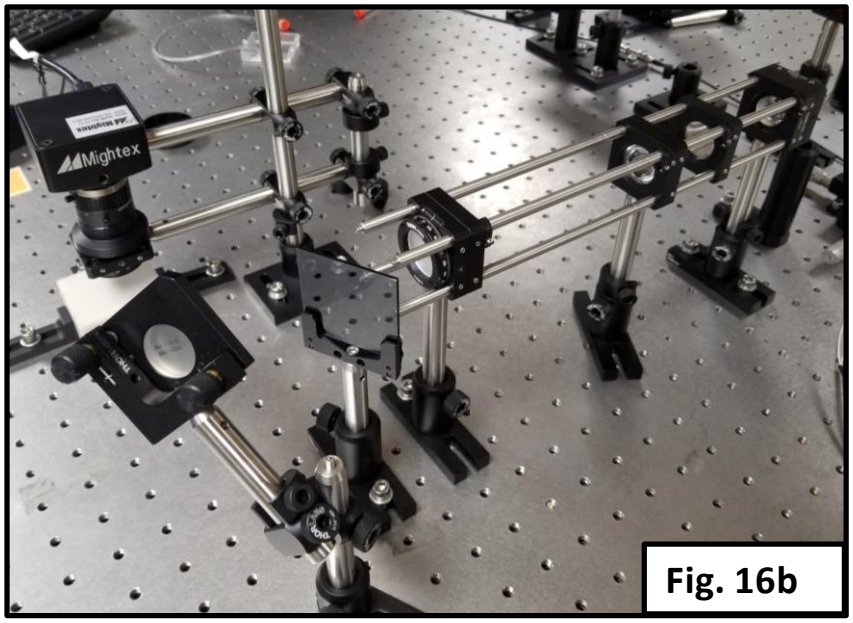

Figure 16. *Fig. 16a provides a schematic of the imaging system that is pictured in Fig. 16b used to collect speckle images. D: Ground diffuser; BE: Beam expander; P_1: Illumination linear polarizer; M: Mirror; P_2: Imaging linear polarizer; C: Camera.*

In front of the imaging lens, a second linear polarizer (LPNIRE100-B; Thorlabs, NJ) was mounted on a rotating mount. This was used to control which polarization was used to image the sample. Three different sets of images were acquired, each having a different angle of polarization. The three states are referred to as- (1) unpolarized, (2) parallel, and (3) cross. The parallel polarization was defined to be the angle at which the intensity of specular reflections from the position of the sample to the camera was maximized. The cross polarization was defined as the polarization angle at 90° to the parallel angle. To capture the unpolarized images, the rotating polarizer was removed from in front of the detector. This met that the imaged light was expected to be *partially-polarized*. The neutral density filter in the illumination path was adjusted to compensate for changes in the intensity when the imaging polarizer was added or

removed from the setup. The power of light reaching the detector was 9.8 μW, 10.8 μW, and 10.3 μW for the unpolarized, parallel, and cross state respectively.

5.2.2- Phantom Construction

Fig. 17 shows a picture of the flow chamber used in this investigation. The flow channel was the same as that described in Section 4.2 and was attached to the bottom surface of a plastic chamber (4.9 cm long x 4.9 cm wide x 1.0 cm tall). The flow channel was attached to a syringe pump that was programed to pump a scattering media through the phantom at various rates, as described below. The flow chamber was fixed on top of a scattering, plastic block that provided a semi-infinite layer beneath the flow. To bury the flow channel at increasing depths, a scattering fluid was added to the flow chamber at constant volumes.

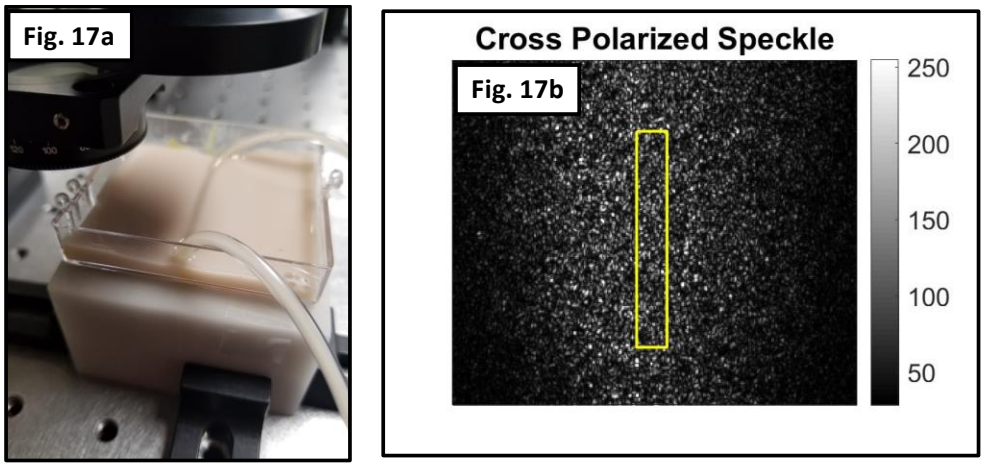

Figure 17. *An image of the flow phantom (Fig. 17a) and captured raw speckle image (Fig. 17b) using cross polarization at the baseline depth (+0.0 mL). The yellow rectangle indicates the ROI in which the mean flow index was found to quantify the LSCI flow measurement.*

The fluid used to flow through the channel and surrounding fluid used to bury the channel were the same. It consisted of 1.0 μm diameter polystyrene microspheres (Polybead microspheres, 07310, Polysciences Inc., Warrington, PA) suspended in deionized water with μ_s' of 12 cm^{-1} at 785 nm as calculated using Mie theory [51] and dissolved bovine hemoglobin (H3760; MilliporeSigma, MO) with μ_a of 0.08 cm^{-1}, measured using a spectrophotometer (Cary 100 UV-Vis, Agilent Technologies, Wilmington, DE).

5.2.3- Data Collection and Analysis

LSCI measurements were collected at 5 different volumes of scattering media added to the chamber. The smallest volume (8 mL) used to bury the flow was determined by adding media to the flow chamber such that the flow channel was just covered by the fluid. Using a fluid to bury the channel limited the precision at which the exact thickness of media covering the top of the

channel could be measured, however it allowed for a simple method to increase the depth. This was accomplished by adding increments of 0.5 mL of the media to the chamber once the baseline depth was determined. Based on the geometry of the chamber, it was estimated that the depth of the channel increased by about 200 μm each time the 0.5 mL of fluid was added to the chamber. The five depths will be indicated by the volume of fluid added to the chamber after the baseline depth. (+0.0 mL, +0.5 mL, +1.0mL, +2.0 mL, and +2.5 mL.). For each depth and polarization, images were captured for 5 pump flow rates ranging from 0 to 8mL/hr (0 to 1.1 mm/s).

Speckle images collected for these experiments were obtained with an exposure time of 6 ms at a frame rate of 30 ms for each depth, flow rate and polarization. 60 frames were captured for each experiment. LSCI analysis was performed over an ROI of 25x150 pixels for each of the raw speckle images acquired. A LSCI flow index, *F*, for each image was calculated using the mean of the inverse of the contrast squared (Eqn. 1.15) within the selected ROI.

A LSCI flow-sensitivity parameter, F_S, was then developed to quantify LSCI's sensitivity to relative changes in flow as a function of polarization and depth using Eq. 5.1. This parameter normalized the change in LSCI's flow measurement for each depth, (*d*), polarization (*p*), and flow (*f*) from the measurement with the pump turned off (i.e. f = 0 mL/hr) to the measured change between pump rates of 8 and 0 mL/hr at the baseline depth (d = +0.0 mL) with the unpolarized imaging.

$$F_S = \frac{F(p,f,d) - F\left(p,0\,\frac{mL}{hr},d\right)}{F\left(unpol.,8\frac{mL}{hr},+0.0\;mL\right) - F\left(unpol.,0\frac{mL}{hr},+0.0mL\right)} = \frac{\Delta F_f^p(d)}{\Delta F_{max}^{unpol.}(d=0)} \tag{5.1}$$

In addition, the speckle images of the flow phantom, a series of static speckle images were captured of the backscattered light from the plastic block on which the flow phantoms were positioned. These images were used to first calculate the average speckle sizes (2.7 pixels/speckle) and examine the statistics of the speckle images of the three polarizations.

5.3- Results and Discussion

According to probability theory, a PDF of a sum of two independent, random variables is the convolution of the PDFs of those two variables [12]. I first present results that examine whether this relation holds true for the assumptions that- (1) the unpolarized speckle intensity images are the sum of the orthogonally polarized images (Eqn. 5.2) and (2) the two orthogonally polarized speckle fields are independent of one another.

$$I_{total} = I_{\perp} + I_{\parallel} \tag{5.2}$$

Fig. 18 shows that PDFs of 100x100 ROIs of the plastic block for the cross, parallel, and unpolarized speckle intensities. This ROI was selected because it was the middle of the illuminated area within the captured image and included the ROI selected to find the mean LSCI measurement was found when the tube was positioned under the camera. It can be observed that the PDFs of the polarized speckle follow that expected negative exponential for intensities greater than about half of the mean intensity, but quickly decay of intensities less that than half the mean (Fig. 18a). The unpolarized speckle PDF does not follow the negative exponential throughout the entire range of intensities (Fig. 18b). In addition, Fig. 18b shows the convolution of the two polarized PDFs (purple). This function has the same shape of the unpolarized PDF, however twice the convolution (green) seems to better match the values of the unpolarized PDF. It is currently unsure why it is double the convolution that matches the unpolarized PDF, however these results could suggest that the unpolarized speckle field is in fact an independent sum of the two polarized speckles.

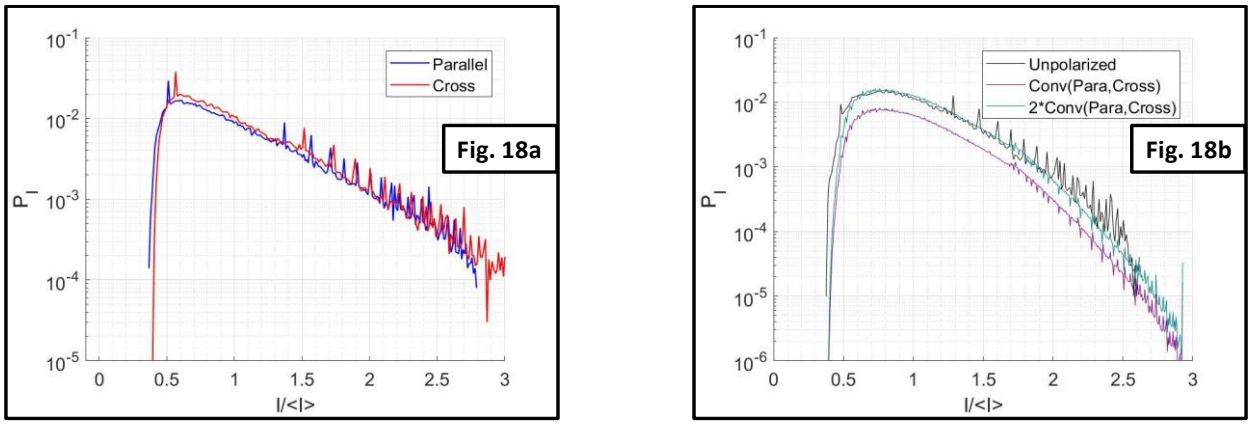

Figure 18. *The figure on the left (Fig. 18a) shows the PDFs of the cross (red) and parallel (blue) static speckle images. The figure on the right (Fig. 18b) shows that of the unpolarized static speckle (black). Fig. 18b also displays the convolution of the two polarized speckle PDFs (purple) as well as twice the convolution (green).*

Next, the results from the LSCI flow measurements of the optical phantom at all three polarization states are presented. The LSCI flow measurements, *F*, are shown as a function of pump flow rate (Fig. 19) and as a function of the volume added to the chamber (Fig. 20). The data markers indicate the mean LSCI flow index across the 60 repeat images at each volume added, polarization, and flow rate combination. The error bars indicate the standard deviation of the flow index across the 60 images. From Fig. 19, it can be observed that the unpolarized speckle had a significantly smaller contrast that the polarized speckle images (indicated by the larger flow measurement values). This means that examining the scattered light in all polarization directions artificially increases the flow measurements relative to using a linear polarization of the scattered field. The cross polarized speckle has a larger mean flow measurement than the parallel speckle, though the difference is not as large as the difference

between either of the polarized measurements and the unpolarized. It can also be observed that the measurements of the flow follow a linear trend with an increasing pump rate from 1 mL/hr to 8 mL/hr at the three displayed depths.

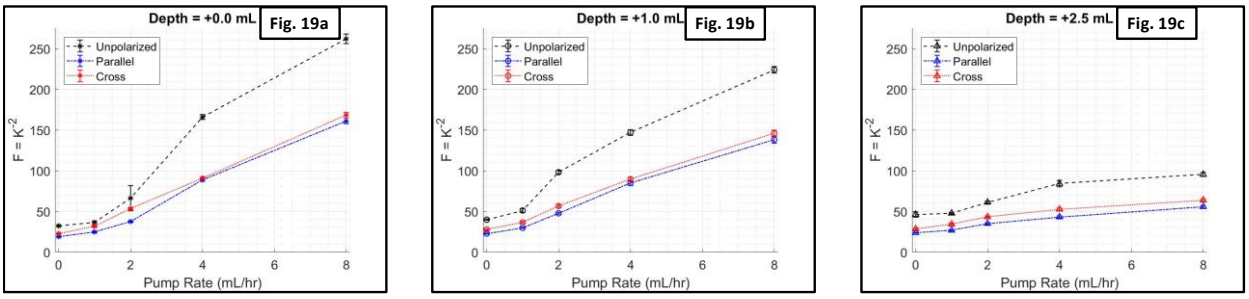

Figure 19. *These figures show the LSCI flow measurements as a function of the pump rate with +0.0 mL, +1.0 mL, and +2.5 mL of surrounding fluid added to the chamber above the baseline depth for the unpolarized (black), parallel (blue), and cross (red) (~400μm depth/1 mL).*

Fig. 20 provides a further investigation of how the measurements changed as a function of depth. From these figures, it can be observed that the relation to depth was dependent on the flow rate of through the tube. With the pump turned off (i.e. 0 mL/hr) adding volume to the chamber increased the LSCI measurements (Fig. 20a). At the highest flow rate (8 mL/hr), the flow measurements decrease for all three polarizations as the depth increased (Fig. 20c). At an intermediate flow rate (2 mL/hr), the measurements peaked at a maximum at a depth of +1.0 mL added to the chamber. These results were very intriguing to observe. The sensitivity parameter defined by Eqn. 5.1 was used to examine these trends.

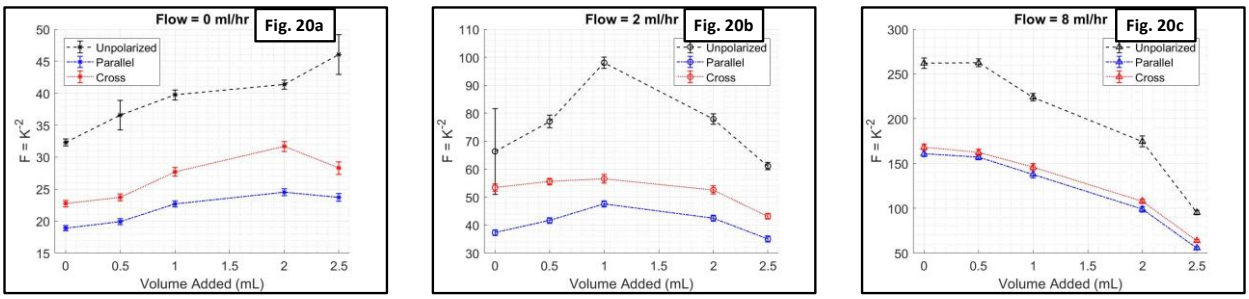

Figure 20. *This set of figures show the LSCI flow measurements as a function of the volume of scattering media added to the chamber above 8 mL at flow rates of 0 mL/hr, 2 mL/hr, and 8 mL/hr through the flow tube for the unpolarized (black), parallel (blue), and cross (red) (~400μm depth/1 mL).*

The sensitivity parameter for all the flow rates (except 0 mL/hr) are shown in Fig. 21. The height of the bars and error bars represent the mean and standard deviation of the F_S across

the 60 frames captured for each combination of volume added, polarization, and flow rate. The color of the bars indicate the volume of media added to the chamber above 8 mL (see legend). The figure is separated into 4 separate bar plots, each one for the 4 pump flow rates (excluding 0 mL/hr). At three flow rates (excluding 1 mL/hr), the unpolarized condition had a larger F_S than the 2 polarized conditions at each depth. This indicates that for the same change in flow rate through the flow channel, the contrast of partially polarized speckle experienced a greater change than the polarized speckle. At the 2 highest flow rates (4 and 8 mL/hr), all the polarizations displayed a downward trend in sensitivity as the depth increased above baseline, suggesting that LSCI's sensitivity to flow rates greater than 4 mL/hr is significantly diminished as the flow is buried by more static media. At 1mL/hr and 2 mL/hr, the unpolarized and parallel polarizations showed an interesting trend in sensitivity. The sensitivity increased from +0.0 mL to a peak at +1.0 mL and then decrease as more scatterers were added to the chamber. The cross polarization was nearly constant from baseline to the +1.0 mL and then declined at +2.0 mL.

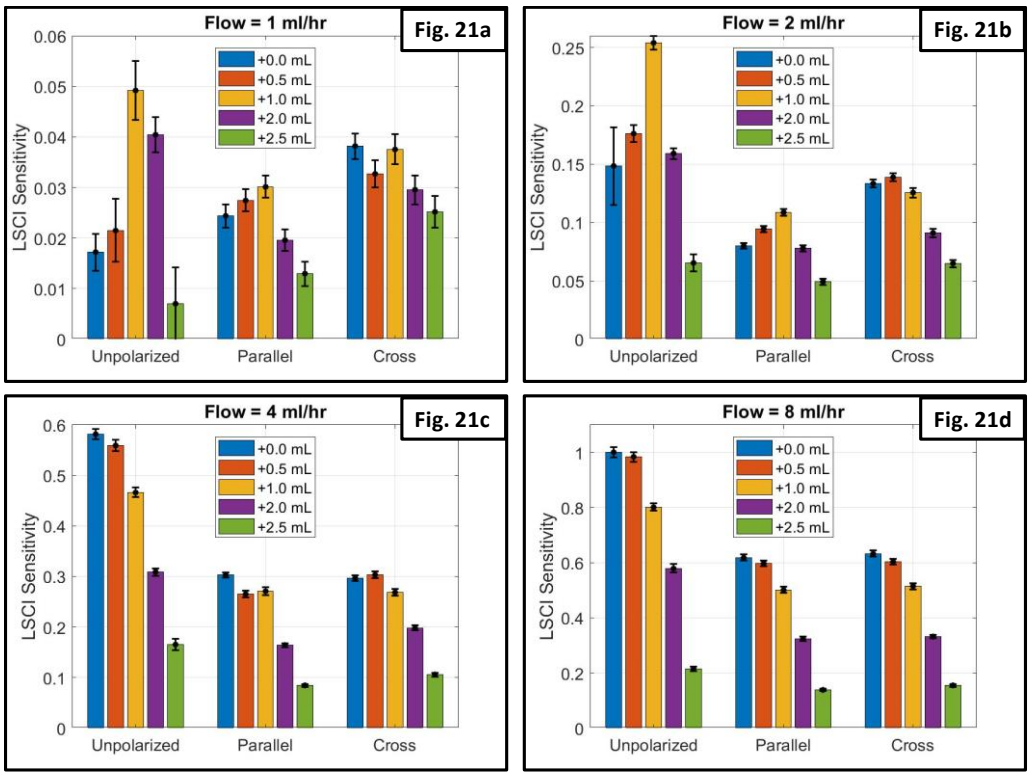

Figure 21. *The four bar plots show the LSCI sensitivity parameter (Eqn. 5.1) for all three polarizations as a function of buried depth (bar color) for four flow rates: 1 mL/hr (Fig. 21a); 2 mL/hr (Fig. 21b); 4 mL/hr (Fig. 21c); 8 mL/hr (Fig. 21d).*

These results demonstrated that many parameters need to be taken into account while using LSCI to sense flow. Both the optical properties of the sample and imaging properties affect LSCI meausrements. This exemplifies why is is difficult for LSCI to be a method of obtaining absolute flow rates. The results displayed in Fig. 19 show that LSCI is able to sense relative flow changes in a constant sample and imaging setup when the imaging is correctly setup. The results

displayed in Fig. 21 show that the LSCI measurements are influenced by the flow rate, buried depth of the flow, and the polarization of light.

Chapter 6 – Future Directions

The most pressing work to be completed is to obtain an understanding of the results discussed in Chapter 5. I hope that the physical explanations of the observed trends, such as those shown in Fig. 20, can be understood. The work is currently being formatted so that it can be published in a peer-reviewed journal such that the results can be shared with the academic community.

There is work that has been begun to continue the work discussed in Chapter 3. An Internal Review Board (IRB) application was submitted to use LSCI to assess PORH to compare the vascular health of individuals that regularly exercise versus individuals that do not. The IRB application #01603r titled *Non-invasive assessment of microvascular function via laser speckle contrast imaging in athletes vs. non-athletes* was resubmitted with revisions to the university and is expected to be approved. This will be a thorough study that hopes to demonstrates LSCI's ability to be applied to biomedical studies.

Flow measurements using DCS were collected during the completion of the work described in Chapter 3 with the hopes of comparing DCS and LSCI. The two techniques possess similar underlying theory. Therefore, it would be intriguing to compare the two methods which vastly differ experimentally. An initial comparison was submitted to *Biomedical Optics Express* but was rejected from publication. It would be intriguing to complete a more thorough comparison of the two techniques in the future.

The prospectus that preceded this thesis proposed that a multi-wavelength LSCI system be constructed. Unfortunately, this was not accomplished in the time of this work. However, I still believe that it would be a useful tool to have. Such a system would allow studies that investigate the effects that the illumination wavelength has on LSCI more efficiently. The difficulty that comes with this task is designing the electrical system that is needed to externally trigger multiple Mightex cameras simultaneously. I would suggest that developing an external trigger system for the camera be one of the next tasks to be completed to better the LSCI set up described in this thesis.

As displayed in the above chapters, many parameters affect LSCI. In Section 1.5, I outlined a few of the variations of LSCI that are being developed by others. It would be of value to investigate how the parameters discussed in this work affect both multi-exposure LSCI and spatial frequency LSCI. However, these techniques do require more complex instrumentation. With the great number of parameters that affect LSCI and the range of variations of the techniques that are being developed, there is no shortage of LSCI research that needs to be completed in the future.

Chapter 7 – Conclusion

In Chapter 1, an introduction and outline of the theory underlying LSCI was presented, and the experimental approach was presented in Chapter 2. Chapter 3 presented an experimental validation of the technique as a blood flow measuring technique that can detect induced changes in flow rates. It was also demonstrated that such measurements are dependent on the wavelength of illumination used to image the sample. This observation of wavelength dependence lead to the work discussed in Chapter 4. The multi-wavelength investigation showed that LSCI flow measurements are significantly affected by the media surrounding the flow. The depth of the flow, optical properties of the surrounding media, and the illumination wavelength impacted the LSCI measurements of the flow through the channel embedded in the optical phantom. Chapter 6 provided a further depth-sensitivity study of LSCI. It demonstrated that the polarization state of the observed scattered light impacts the flow measurements and that the sensitivity of the flow is a function of both the buried depth and flow rate.

An important experimental adjustment was made between the study outlined in Chapter 4 and Chapter 5. In Chapter 4, the flow rate through the channel was 0 mL/min, 3 mL/min, and 6 mL/min, and the exposure time of the camera was 10 ms. One of the negative results observed using these parameters was that LSCI could not confidently distinguish between the 3 mL/min and 6 mL/min. For this reason, the flow rates were decreased to range from 0 mL/hr to 8 mL/hr (a decrease by a factor amount 60 compared to the study outlined in Chapter 4). The exposure time was also decreased in Chapter 5 to 6 ms. As shown in Fig. 18, LSCI was able to significantly distinguish between the flow rates and displayed a linear relationship. As discussed in Section 2.2.2, LSCI is dependent on the ratio between the exposure time and the flow rate of the scattereres. By varying the flow rates and exposure time, the LSCI's ability to detect changes in flow was increased. This is just one example of how LSCI is dependent on a complex relationship between many parameters.

This thesis shows experimental results that demonstrate the dependence of LSCI's sensitivity to flow on the depth of the flow, the optical properties of the surrounding media, and polarization of light. Each of these parameters and many more must be considered to optimize LSCI's sensitivity to flow.

APPENDICIES

A. Speckle Simulation

This appendix contains a MATLAB function that simulates a fully-developed speckle pattern.

```
function [speckle] = speckle_sim(N, r);

%function [speckle] = speckle_sim(N, r);
%
%This function generates simulated speckle. Following the discription
of:
%Duncan, et. al "Statistics of local speckle contrast." J. Opt. Soc.
Am.
%(2008)
%
%Inputs:
%   N = the length of the final NxN matrix of the speckle filed.
%   r = parameter controlling the size of the speckle (2r = N; speckle
=
%   2*pixels) (larger r = smaller speckle)
%
%Outputs:
%   speckle = NxN array of simulated speckle

[x,y] = meshgrid(1:N);
c = double(sqrt((x-N/2).^2+(y-N/2).^2)<=r); %select circular region
a = fft2(c.*exp(1i*(2*pi.*rand(N)-pi))); %fill with random phasor
speckle = a.*conj(a);
speckle = speckle./max(speckle); %normalize intensity value

figure(1);clf;
imagesc(speckle);
colormap('gray');
```

B. Speckle Size Calculation

This appendix contains a MATLAB function that estimates the mean speckle size of a static speckle image.

```
function [H_spec, V_spec,H_norm_cov, V_norm_cov,lag_H,fitH,
fitH_stats,  lag_V, fitV, fitV_stats] = OSIM_specklesize(I)
%function [H_spec, V_spec,H_norm_cov, lag_H,fitH, fitH_stats,
V_norm_cov, lag_V, fitV, fitV_stats] = OSIM_specklesize(I)
%
%Outputs the normalized autocovariance of the matrix I for each
%each column of I, producing the autocovariance function. The FWHM of
this
%function is related to the mean horizontal speckle width present in
I.
%This function plots the reulting autocovariance, a best fit to a
Gaussian,
%and the autocovariance produced by Mathworks SpeckleSize function.

I = double(I);

[H_norm_cov,lag_H, V_norm_cov,lag_V] = OSIM_autocov(I);

% H_inds = find(H_norm_cov >= 0);
% V_inds = find(V_norm_cov >= 0);

gauss1 = fittype('gauss1');
[fitH, fitH_stats] = fit(lag_H(lag_H>=-3 &
lag_H<=3)',H_norm_cov(lag_H>=-3 & lag_H<=3)',gauss1);
[fitV, fitV_stats] = fit(lag_V(lag_V>=-3 &
lag_V<=3)',V_norm_cov(lag_V>=-3 & lag_V<=3)',gauss1);

H_coef = coeffvalues(fitH);
H_sigma = sqrt(H_coef(3));
H_spec = 2*sqrt(2*log(2))*H_sigma;
% disp(sprintf('Horizontal Speckle Size = %0.2f pixels', H_spec));

V_coef = coeffvalues(fitV);
V_sigma = sqrt(V_coef(3));
V_spec = 2*sqrt(2*log(2))*V_sigma;
% disp(sprintf('Vertical Speckle Size = %0.2f pixels', V_spec));

end
%=========================================================================
function [H_norm_cov,lag_H, V_norm_cov, lag_V] = OSIM_autocov(I)

%function [H_norm_cov,lag] = OSIM_autocov(I)
%
%Produces the autocovariance function of the row (or column) vector I
by
%computing the correlation function of I reduced by mean(I)
```

```
mean_I = mean(I(:));
I_reduced = I - mean_I;
[H_cov,lag_H, V_cov, lag_V] = OSIM_autocorr(I_reduced);
H_norm_cov = H_cov/max(H_cov);
V_norm_cov = V_cov/max(V_cov);

end
%=========================================================================
function [H_corr,lag_H,V_corr,lag_V] = OSIM_autocorr(I);
[N,M] = size(I);
%Calc the correlation by sliding the intesity image horizontally
across
%itself
I_f_H = zeros(N,3*M-2);
I_f_H(:,M:2*M-1) = I;
H_corr = zeros(1,2*M-1);
H_corr_row = zeros(1,2*M-1);
for n = 1:N
    for m = 1:2*M-1
        A_H = I(n,:).*I_f_H(n,m:m+M-1); %multiply overlapping rows
together
        H_corr_row(1,m) = sum(A_H(:));%Sum product across the row
    end
    H_corr = H_corr + H_corr_row; %Sum correlation down column
end
lag_H = -(M-1):(M-1);
%Calc the correlation by sliding the intesity image vertically across
%itself
I_f_V = zeros(3*N-2,M);
I_f_V(N:2*N-1,:) = I;
V_corr = zeros(1,2*N-1);
V_corr_col = zeros(1,2*N-1);
for m = 1:M
    for n = 1:2*N-1
        A_V = I(:,m).*I_f_V(n:n+N-1,m); %multiply overlapping columns
together
        V_corr_col(1,n) = sum(A_V(:));
    end
    V_corr = V_corr + V_corr_col;
end
lag_V = -(N-1):(N-1);
end
```

C. Speckle Contrast Calculations

This appendix contains a MATLAB functions used to calculate the speckle contrast.

C.1 Original LSCI Function

This MATLAB function uses for loops to calculate the contrast within each spatial window.

```
function [contrast_K, flow_map, evpome_im] = lasca_original(fname, pt,
offset, wsize)

%function [contrast_K] = lasci_analysis(fname, pixelsize, p1, offset)
%
%This function allows a user to preform a speckle contrast analysis on
%a rectangular ROI of an image designated by a single point
%(p1) and lengths given by [offset(1),offset(2)]. It loops
%through each x and y pixel
%
%inputs:
%fname = name of image or previously read intensity image
%windowsize = size of LSCI sliding window (7x7 default)
%p1 = top right corner coordinate of ROI
%offset = x and y length of ROI
%
%outputs:
%flow_img = 2D matrix of flow values

if ~exist('wsize1', 'var') %if not inputted, window is 7x7
    wsize = 7;
end
if isa(fname,'char')
    raw_im = double(imread(fname));
else
    raw_im = double(fname);
end
if ~exist('pt','var')
    pt = [4 4]; %entire image
end
if ~exist('offset','var')
    size_im = size(raw_im);
    offset = [size_im(2), size_im(1)]-[8 8]; %entire image
end

xr = [pt(1) pt(1)+offset(1) pt(1)+offset(1) pt(1) pt(1)];
yr = [pt(2) pt(2) pt(2)+offset(2) pt(2)+offset(2) pt(2)];

evpome_im = double(raw_im);
xrange = floor(xr(1)):floor(xr(2));
yrange = floor(yr(1)):floor(yr(3));
add_offset = unique(round([ceil(-wsize/2):0.5:floor(wsize/2)]));
%find range of sliding window in which to find contrast
xind = 0;
for x=xrange %loop through each pixel
```

```
    xind = xind+1;
    yind = 0;
    for y=yrange
        pix_x = (x)+add_offset;
        pix_y = (y)+add_offset;
        im_sl = evpome_im(pix_y, pix_x);
        yind = yind+1;
        mean_I = mean(im_sl(:));
        contrast_K(yind, xind) = std(im_sl(:), 1)./mean_I;
        %calclate the contrast for each pixel
    end;
end
flow_map = 1./contrast_K.^2; %Calc flow
end
```

C.2 Updated LSCI Function

This MATLAB function provides a more efficient method of finding the speckle contrast.

```
function [K,flow_map,I] = GetLSCI_OSIM(fname, ws, fig_num, pt,offset)

%function [K,flow_map,I] = GetLSCI_OSIM(fname, ws, fig_num, pt,offset)
%
%Updated 5/16/2018 by Anthony Young
%
%This function generates a LSCI flow map from an inputted raw image.
%Instead of sliding a window (ws-by-ws) around each pixel, this
function
%generates a 3-dim matrix where each layer is the selected ROI of
%intensities shifted by 1 row or column.
%Input:
%   fname = either the name of the raw file or the matrix of the read
image
%   pt = top left point of ROI [x1,y1]
%   offset = size of the ROI [xrange, yrange]
%   ws = window size of sliding window (7 by default)
%
%Output:
%   flow_map = LSCI flow map

if ~exist('fig_num', 'var')
    fig_num = 1;
end
if ~exist('ws', 'var') %if not inputted, window is 7x7
    ws = 7;
end

if isa(fname,'char')  %can input image filename or read image
    raw_I = double(imread(fname));
else
    raw_I = double(fname);
end
```

```
if ~exist('pt','var')
    pt = ceil(ws./2) + [0 0]; %overestimate the overhang in ROI
end
if ~exist('offset','var')
    size_im = size(raw_I);
    offset = size_im(2:-1:1)-2.*pt;
end

xr = [pt(1) pt(1)+offset(1) pt(1)+offset(1) pt(1) pt(1)];
yr = [pt(2) pt(2) pt(2)+offset(2) pt(2)+offset(2) pt(2)];


xrange = floor(xr(1)):floor(xr(2));
yrange = floor(yr(1)):floor(yr(3));

I = zeros(length(yrange), length(xrange), ws^2);
%create ws^2 nbym matrices each with select_I shifted about sliding
window

shift_inds = unique(round([ceil(-ws/2):0.5:floor(ws/2)]));
count = 1;
for xs = shift_inds
    for ys = shift_inds
                I(:,:,count) = raw_I(yrange+ys,xrange+xs); %shift and
add to the 3rd dim
        count = count+1;
    end
end

K = std(I,1,3)./mean(I,3); %Calculate contrast
flow_map = 1./K.^2; %Calc flow

end
```

D. Instructions for Using Mightex Camera

In this appendix, I present instructions on how to use the software that operates the Mightex camera (SME-B012-U; Mightex Systems, Pleasanton, CA) used to capture the speckle images for this thesis. Fig. 22 contains a screenshot of the software's user interface that I reference while explaining how to operate and change the settings of the camera. The numbers in the figure highlight specific buttons or controls.

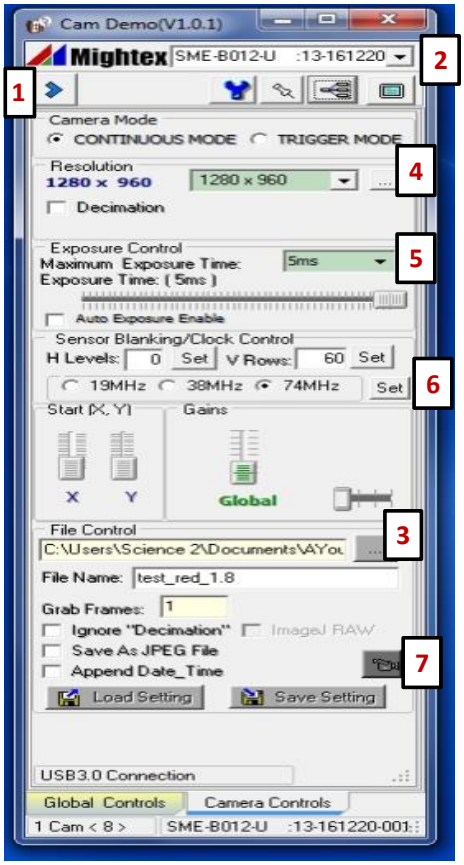

Figure 22. *A screenshot of the user interface for the Mightex camera (SME-B012-U). The red numbers indicate the buttons referenced in Appendix D.*

1. Once the camera is securely mounted, connect the USB cord to the ontrolling computer using a USB cord.
2. Launch the *SSClassicCameraApp* application.
3. Select camera being used (i.e. **SME-B012-U**) and **8 Bit** in the first window that pops up and click **ok**.
4. Turn the detector on by clicking the blue arrow button at the top left of the camera's interface ***#1***. The button will turn into a red circle.

5. Open the window viewer by clicking on ***#2***. This will allow the user to view the image that the camera is capturing.
6. Focus the camera on the flow sample and adjust the aperture to the desired f-number.
7. Select the control file by clicking on ***#3***. This will be the folder to which the captured images will be saved.
8. Enter the file name of the image in the field next to "File Name:".
9. Select the number of frames to grab in the field next to "Grab Frames." The software will save repeat images with the frame number appended to the end of the file name.
10. Select the resolution of the image using ***#4***. A larger resolution will increase the field of view within the captured image, but also increase the size of the file.
11. Set the exposure time. ***#5*** is a drop-down menu that controls the range of exposure times that can be set using the slide control underneath the menu. Be careful not to have an exposure time that saturates the camera!
12. Fix the frame rate. The frame rate is controlled by the H Level, V Rows, and that is selected at ***#6***. To calculate the frame rate, click on the blue wrench button ***#7*** and open the preferences menu. The frame rate is the sum of the *Frame Read Time* and *Actual VBlanking* times.
13. To capture the images, click on the Grab Frames button ***#7***.

    NOTE: Camera setting may be saved and loaded using the respective buttons at the bottom of the user interface window.

BIBLIOGRAPHY

1. J. W. Goodman, "Some Fundamental Properties of Speckle," Journal of the Optical Society of America **66**, 1145-1150 (1976).
2. J. W. Goodman, "Speckle Phenomena in Optics," (Roberts and Company, Greenwood Village, CO, 2007).
3. A. E. E. J. C. Dainty, M. Francon, J. W. Goodman, T. S. McKechnie, G. Parry, "Laser speckle and related phenomena.," Applied optics **23**, 2661 (1984).
4. D. A. Boas and A. K. Dunn, "Laser speckle contrast imaging in biomedical optics," J. Biomed. Opt. **15**, 12 (2010).
5. A. F. Fercher and J. D. Briers, "Flow visualization by means of single-exposure speckle photography," Optics Communications **37**, 326-330 (1981).
6. J. D. B. S. Webster, "Laser speckle contrast analysis (LASCA): A nonscanning full-field technique for monitoring capillary blood flow," J. Biomed. Opt. **1**, 174-179 (1996).
7. D. Briers, D. D. Duncan, E. Hirst, S. J. Kirkpatrick, M. Larsson, W. Steenbergen, T. Stromberg, and O. B. Thompson, "Laser speckle contrast imaging: theoretical and practical limitations," J Biomed Opt **18**, 066018 (2013).
8. P. G. Vaz, A. Humeau-Heurtier, E. Figueiras, C. Correia, and J. Cardoso, "Laser Speckle Imaging to Monitor Microvascular Blood Flow: A Review," IEEE reviews in biomedical engineering **9**, 106-120 (2016).
9. J. W. Goodman, *Speckle phenomena in optics: theory and applications* (Roberts and Company Publishers, Greenwood Village, CO, 2007).
10. J. W. Goodman, "Random Walk with a Large Number of Independent Steps," in *Speckle Phenomena in Optics: Theory and Applications* (Roberts and Company Publishers, Greenwood Village, CO, 2007).
11. F. L. Pedrotti, L. S. Pedrotti, and L. M. Pedrott, *Intoduction to Optics* (Pearson, Upper Saddle River, NJ, 2007).
12. J. W. Goodman, *Statistical Optics,* Wiley Classics Library ed. (John Wiley & Sons, New York, NY, 1985).
13. J. W. Goodman, "Statistical properties of laser speckle patterns," in *Laser Speckle and Related Phenomena*, J. C. Dainty, ed. (Springer-Verlag, Berlin, 1975), pp. 9-75.
14. J. D. Briers and A. F. Fercher, "RETINAL BLOOD-FLOW VISUALIZATION BY MEANS OF LASER SPECKLE PHOTOGRAPHY," Invest. Ophthalmol. Vis. Sci. **22**, 255-259 (1981).
15. J. C. Ramirez-San-Juan, R. Ramos-Garcia, I. Guizar-Iturbide, G. Martinez-Niconoff, and B. Choi, "Impact of velocity distribution assumption on simplified laser speckle imaging equation," Opt. Express **16**, 3197-3203 (2008).
16. K. Khaksari, Kirkpatrick, S. J., "Laser speckle modeling and simulation for biophysical dynamics: influence of sample statistics," J. of Biomedical Photonics & Eng **3**(2017).
17. D. D. Duncan, S. J. Kirkpatrick, and R. K. K. Wang, "Statistics of local speckle contrast," J. Opt. Soc. Am. A-Opt. Image Sci. Vis. **25**, 9-15 (2008).

18. R. Bandyopadhyay, A. S. Gittings, S. S. Suh, P. K. Dixon, and D. J. Durian, "Speckle-visibility spectroscopy: A tool to study time-varying dynamics," Rev. Sci. Instrum. **76**, 11 (2005).
19. A. B. Parthasarathy, W. J. Tom, A. Gopal, X. J. Zhang, and A. K. Dunn, "Robust flow measurement with multi-exposure speckle imaging," Opt. Express **16**, 1975-1989 (2008).
20. B. J. Berne and R. Pecora, *Dynamic Light Scattering: with Applications to Chemistry, Biology, and Physics* (Dover Publications, Mineola, NY, 2000).
21. D. D. Duncan and S. J. Kirkpatrick, "Can laser speckle flowmetry be made a quantitative tool?," J. Opt. Soc. Am. A-Opt. Image Sci. Vis. **25**, 2088-2094 (2008).
22. K. Khaksari and S. J. Kirkpatrick, "Laser speckle contrast imaging is sensitive to advective flux," J. Biomed. Opt. **21**, 8 (2016).
23. I. Cordovil, G. Huguenin, G. Rosa, A. Bello, O. Kohler, R. de Moraes, and E. Tibirica, "Evaluation of systemic microvascular endothelial function using laser speckle contrast imaging," Microvasc. Res. **83**, 376-379 (2012).
24. M. Roustit, C. Millet, S. Blaise, B. Dufournet, and J. L. Cracowski, "Excellent reproducibility of laser speckle contrast imaging to assess skin microvascular reactivity," Microvasc. Res. **80**, 505-511 (2010).
25. A. Ponticorvo and A. K. Dunn, "How to Build a Laser Speckle Contrast Imaging (LSCI) System to Monitor Blood Flow," Journal of Visualized Experiments : JoVE (2010).
26. A. Young and K. Vishwanath, "Quantitative assessment of reactive hyperemia using laser speckle contrast imaging at multiple wavelengths," in *Conference on Dynamics and Fluctuations in Biomedical Photonics XIII*, Proceedings of SPIE (Spie-Int Soc Optical Engineering, 2016),
27. A. Della Rossa, A. d'Ascanio, M. Cagnoni, C. Stagnaro, A. Parma, M. Mosca, and S. Bombardieri, "Post-Occlusive Reactive Hyperemia (PORH) Test Mirrors Vascular Changes in Systemic Sclerosis (SSc): a Laser Speckle Contrast (LASCA) Study," Arthritis & Rheumatology **66**, S1186-S1186 (2014).
28. M. Draijer, E. Hondebrink, T. van Leeuwen, and W. Steenbergen, "Review of laser speckle contrast techniques for visualizing tissue perfusion," Lasers in medical science **24**, 639-651 (2009).
29. A. Khalil, A. Humeau-Heurtier, G. Mahe, and P. Abraham, "Laser speckle contrast imaging: age-related changes in microvascular blood flow and correlation with pulse-wave velocity in healthy subjects," J. Biomed. Opt. **20**(2015).
30. J. D. Briers and A. F. Fercher, "RETINAL BLOOD-FLOW VISUALIZATION BY MEANS OF LASER SPECKLE PHOTOGRAPHY," Investigative Ophthalmology & Visual Science **22**, 255-259 (1982).
31. A. K. Dunn, "Laser Speckle Contrast Imaging of Cerebral Blood Flow," Ann. Biomed. Eng. **40**, 367-377 (2012).
32. C. Ayata, A. K. Dunn, Y. Gursoy-Ozdemir, Z. H. Huang, D. A. Boas, and M. A. Moskowitz, "Laser speckle flowmetry for the study of cerebrovascular physiology in normal and ischemic mouse cortex," J. Cereb. Blood Flow Metab. **24**, 744-755 (2004).
33. O. Yang and B. Choi, "Laser speckle imaging using a consumer-grade color camera," Opt. Lett. **37**, 3957-3959 (2012).

34. I. Fredriksson and M. Larsson, "On the equivalence and differences between laser Doppler flowmetry and laser speckle contrast analysis," J. Biomed. Opt. **21**, 11 (2016).
35. G. Q. Yu, "Diffuse Correlation Spectroscopy (DCS): A Diagnostic Tool for Assessing Tissue Blood Flow in Vascular-Related Diseases and Therapies," Curr. Med. Imaging Rev. **8**, 194-210 (2012).
36. K. Khaksari and S. J. Kirkpatrick, "Combined effects of scattering and absorption on laser speckle contrast imaging," J. Biomed. Opt. **21**(2016).
37. M. A. Davis, S. M. S. Kazmi, and A. K. Dunn, "Imaging depth and multiple scattering in laser speckle contrast imaging," J. Biomed. Opt. **19**, 10 (2014).
38. J. D. B. S. Webster, "Quasi real-time digital version of single-exposure speckle photography for full-field monitoring of velocity or flow fields," Optics Communications **116**, 36-42 (1995).
39. J. C. Ramirez-San-Juan, C. Regan, B. Coyotl-Ocelotl, and B. Choi, "Spatial versus temporal laser speckle contrast analyses in the presence of static optical scatterers," J. Biomed. Opt. **19**, 5 (2014).
40. T. B. Rice, E. Kwan, C. K. Hayakawa, A. J. Durkin, B. Choi, and B. J. Tromberg, "Quantitative, depth-resolved determination of particle motion using multi-exposure, spatial frequency domain laser speckle imaging," Biomed. Opt. Express **4**, 2880-2892 (2013).
41. S. Yuan, A. Devor, D. A. Boas, and A. K. Dunn, "Determination of optimal exposure time for imaging of blood flow changes with laser speckle contrast imaging," Applied Optics **44**, 1823-1830 (2005).
42. J. C. Ramirez-San-Juan, E. Mendez-Aguilar, N. Salazar-Hermenegildo, A. Fuentes-Garcia, R. Ramos-Garcia, and B. Choi, "Effects of speckle/pixel size ratio on temporal and spatial speckle-contrast analysis of dynamic scattering systems: Implications for measurements of blood-flow dynamics," Biomed. Opt. Express **4**, 1883-1889 (2013).
43. S. J. Kirkpatrick, D. D. Duncan, and E. M. Wells-Gray, "Detrimental effects of speckle-pixel size matching in laser speckle contrast imaging," Opt. Lett. **33**, 2886-2888 (2008).
44. H. Lin, "Speckle mechanism in holographic optical coherence imaging," (University of Missouri, 2009).
45. P. O. Bonetti, G. M. Pumper, S. T. Higano, D. R. Holmes, J. T. Kuvin, and A. Lerman, "Noninvasive identification of patients with early coronary atherosclerosis by assessment of digital reactive hyperemia," Journal of the American College of Cardiology **44**, 2137-2141 (2004).
46. Y. Higashi, S. Sasaki, K. Nakagawa, H. Matsuura, G. Kajiyama, and T. Oshima, "Effect of the angiotensin-converting enzyme inhibitor imidapril on reactive hyperemia in patients with essential hypertension: Relationship between treatment periods and resistance artery endothelial function," Journal of the American College of Cardiology **37**, 863-870 (2001).
47. S. Hagisawa, J. C. Barbenel, and R. M. Kenedi, "INFLUENCE OF AGE ON POSTISCHEMIC REACTIVE HYPEREMIA," Clinical Physics and Physiological Measurement **12**, 227-237 (1991).
48. A. Philpott and T. J. Anderson, "Reactive hyperemia and cardiovascular risk," Arteriosclerosis Thrombosis and Vascular Biology **27**, 2065-2067 (2007).

49. K. Vishwanath and M. A. Mycek, "Polystyrene microspheres in tissue-simulating phantoms can collisionally quench fluorescence," Journal of Fluorescence **13**, 105-108 (2003).
50. K. Vishwanath, W. Zhong, M. Close, and M.-A. Mycek, "Fluorescence quenching by polystyrene microspheres in UV-visible and NIR tissue-simulating phantoms," Opt. Express **14**, 7776-7788 (2006).
51. H. I. W. L. V. Wang, "Raleigh theory and Mie theory for single scatterer," in *Biomedical optical principles and imaging* (John Wiley & Sons, 2007).
52. A. Young and K. Vishwanath, "Investigating the depth-sensitivity of laser speckle contrast imaging in flow phantoms," in *SPIE Medical Imaging*, (SPIE, 2018), 6.
53. M. A. H. a. J. B. Marion, "Reflections and Refraction," in *Classical Electromagnetic Radiation* (Academic Press, Inc., New York, NY, 1994), pp. 163-169.